Polish Academy of Sciences
Institute of Physics

Ph. D. Dissertation

Theory of magnetic properties based on atomic *p*-orbitals in perfect and defected solids

Oksana Volnianska

Supervisor
Prof. Piotr Bogusławski

Warsaw 2009

ACKNOWLEDGEMENTS

I would like to thank my supervisor, Prof. Piotr Bogusławski for his help during this work.

The calculations computations were partially performed at ICM at Interdisciplinary Center for Mathematical and Computational Modeling, Warsaw University.

The research was supported by Program of Fellowships under the Polish National Commission for UNESCO (2009), Grant № 758, and by of Polish Ministry of Science, Grant № 202103036 and Grant № 202 172935.

Contents

Part I

Introduction

In 1928 Heisenberg postulated that magnetism in solids is due to the presence of transition metal or rare earth atoms with partially filled and spin-polarized *d* or *f* electronic shells. Indeed, practically all magnetic systems studied or applied in devices contain transition metal or rare earth ions. Recently however, this paradigm was questioned. In fact, magnetism was experimentally observed or theoretically predicted to exist in a number of systems containing only *s* and *p* electrons. These systems can be divided into two classes. In the first one, spin moments are provided by host atoms that form an ideal bulk crystal. In the second class, spin moments are provided by defects, typically vacancies, or (non-magnetic) dopants in a non-magnetic host. My thesis deals with both ideal bulk crystals that exhibit magnetism of either atomic or molecular origin and with some aspects of the local spin polarization related with vacancies. This is because one of the main goals of this Thesis is to demonstrate that the physical origin of both effects is the same, and consists in the strong spin polarization of *p* orbitals of light atoms from the second row of the periodic table. Below, a review of the results related directly to this Thesis is given. Since this field is already vast and rapidly growing, the results obtained for other systems are also mentioned, but the given literature is not exhaustive.

1.1. Ferromagnetic bulk solids without transition metal atoms

The class includes the defect-free bulk materials containing atoms with partially filled *p* orbitals [1-5]. In Ref. [1] Kukasabe *et al*. have theoretically analyzed CaP, CaAs, and CaSb in the zinc-blende (*zb*) structure by first-principles calculations, and found that they are half-metals with a total spin polarization of holes in the valence band. (Half-metals are metals with a total spin polarization of free carriers on the Fermi level.) Properties of several II^A-V compounds have been further explored in Refs. [2, 3] where it was shown that a number of II^A-V crystals can be half-metals. Similar results were obtained for the *zb* phase of II-C carbides [6]. However, the *zb* structure analyzed in detail in Refs. [1-3] is not the stable crystalline phase of these compounds. The question therefore arises what are the stable

phases, and whether the spin polarization persists in these structures. In fact, II-V compounds crystallize in variety of structures, the most common being Zn_3P_2 or a more complex Zn_3As_2 phases [7]. Magnetic II^{TM}-V compounds (where II^{TM} is a transition metal ion) usually crystallize in the *NiAs* structure [8, 9]. SrN has been observed both in the rock salt (*rs*) [10] and in the monoclinic structure [11, 12]. In fact, it was shown that the *rs* phase is more stable than *zb* [4, 5], and CaN, SrN, and BaN in this structure are ferromagnetic.

The explanation of the presence of non-vanishing spin polarization in various II^{A}-V compounds have been provided in Ref. [4], and the details are given in Part III. The effect originates in the strong spin polarization of light atoms from the second row of the Periodic Table [4], in which a strong Hund's coupling take place. The spin polarization is not destroyed by the formation of bonds in the crystal. In other words, the atomic polarization is stronger that hybridization effects.

Magnetism in ideal bulk compounds can also occur in systems containing O_2 or N_2 dimers in the appropriate charge state, in which the magnetic moments of dimers are not zero. A prototype case is that of molecular magnetism in solid O_2 at low temperature [13], which orders antiferromagnetically with the Neel temperature of 24 K. In fact, this is one of very few cases in which magnetism without transition metal or rare earth ions exists. Recently, magnetism of molecular origin was predicted for Rb_4O_6 that contains O_2 molecules [14-16]. Experiment [16] shows that the effective magnetic moment per hyperoxide unit in Rb_2O_6, 1.83 μ_B, is in a reasonable agreement with the predicted 2 μ_B [14, 15], and the crystal exhibits a frustrated magnetic order [16]. In Ref. [17] we showed that similar molecular magnetism takes place in bulk monoclinic *m*-SrN, in which one half of N ions form N_2 dimers. Magnetic properties of *m*-SrN are analyzed in detailed in Part IV.

1.2. Magnetism in non-magnetic hosts with non-magnetic defects or dopants

A second class of materials in which magnetism can exist without transition metal atoms are crystals, in which spin moments are provided either by dopants or defects. In fact, impurities and defects such as vacancies in insulators typically introduce deep levels in the band gap, and electrons that occupy these levels form states with total spin 0 or 1/2. In the

latter case, magnetic phases are possible provided that the defect concentration is high enough to enable for the magnetic coupling between defects.

1.2.1. Impurity-induced magnetism

This case comprises II-VI (ZnO, MgO, CaO, SrO) and III-V compounds (GaN) doped by light atoms (C, N), and by Cu ions that nominally are non-magnetic because of their closed-shell d^{10} configuration. The first experimental observation of FM in a doped semiconductor was performed by Pan *et al*. [18] They analyzed ZnO containing 1-5 % of C, and found FM at room temperature with the magnetic moment of about 1 μ_B per C atom. Their theoretical results showed that FM is due to the spin polarization of electrons in the C-induced impurity band, and that the presence of additional holes can enhance FM. Indeed, Ye *et al*. observed that co-doping with nitrogen enhances magnetism of ZnO:C powder and their results indicated that magnetism mediated by itinerant electrons may explain the ferromagnetic nature of ZnO:C [19]. Room-temperature FM was also reported for N-doped ZnO [20]. Finally, experimental results showed that a substitution of nitrogen for oxygen in nonmagnetic SrO oxide leads to a holes in *p*(N) states that form local magnetic moments [21]. The nitrogen 1s core-level XPS was used to examine the spin polarization. For $SrO_{0.75}N_{0.25}$ the observed energy separation between singlet and triplet peaks is 1.6 eV, which is consistent with 1.5 eV found in NO which has a spin ½ localized mainly on N.

The mechanism of ferromagnetism in nitrogen-doped ZnO was analyzed by first principle calculations Shen *et al*. [22]. The long-range magnetic coupling was attributed to *p-p* coupling involving holes (similar to the *p-d* exchange coupling), which is derived from the similar symmetry and wave function between the impurity (*p*-like t_2) and valence *p* states. Kenmochi *et al*. have proposed that such an effect takes place also in other oxides doped with carbon [23]. According to their calculations, MgO, CaO, and SrO containing a few per cent of C, which is a double acceptor when substituting O, is ferromagnetic due to the spin polarization of carriers in the C-induced impurity band. Thus, the driving force for FM in these systems is the same as in the case of II-V and II-C ideal crystals.

Finally, I note that magnetic 3*d* transition-metal doped diluted magnetic semiconductors based on III-V and II-VI hosts also have been extensively studied due to their potential application in spintronics [24, 25]. Recently, however, FM was also observed in

ZnO doped with Cu [26-34] and in Cu-doped in GaN [35, 36]. These results are unexpected because Cu ions, which have $3d^{10}$ electrons in the closed-shell configuration, are nominally non-magnetic [30, 31, 33].

From the theoretical side, first studies found that ZnO:Cu (25 %) is nonmagnetic [26]. However, calculations for lower doping levels indicated ZnO doped with 6.25 % [27] and 3.125 % Cu [28] should be ferromagnetic. The influence of defect charge state on the magnetism ZnO:Cu as well as the Cu defects clustering were investigated by first-principles calculations by D. Huang *et al*. [37]. It was demonstrated that *p*-type ZnO:Cu is expected to be ferromagnetic, but in *n*-type ZnO:Cu the magnetic moment of Cu vanishes. Furthermore, neutral substitutional Cu impurities are found to have a tendency to clustering, which maintains the FM ordering. And finally, Ye *et al*. [38] and Huang *et al*. [39] both found that ZnO:Cu is FM.

In parallel, intensive experimental research started in this field, but the present situation is confusing. The magnetic circular dichroism spectra of ZnO:Cu (0.3 %) suggested that it is a diluted magnetic semiconductor [29]. Additionally, a saturable component of the magnetization was observed in M-H curves of ZnO powders doped with 2 % and 5 % Cu and was interpreted as ferromagnetism [30]. Buchholz *et al*. grown a series of ZnO:Cu films by pulsed-laser deposition [31]. They showed that ZnO:Cu (1%) film has the Curie temperature of about 390 K, and the saturation magnetization at 200 K corresponds to a magnetic moment of 0.4 μ_B per copper atom. Keavney *et al*. [32] has reported X-ray absorption spectroscopy (XAS) and magnetic circular dichroism (XMCD) studies of the films like in Ref. [31]. Surprisingly, however, authors find that the ferromagnetic spin polarization does not reside on the Cu 3*d*, O 2*p*, Zn 4*s*, or Zn 3*d* states. They find a small paramagnetic contribution on the Cu 3*d* states which is more pronounced at the surface of the films. Keavney *et al*. found FM in *p*-type ZnO:Cu but not in *n*-type ZnO:Cu sample. Next, ZnO films with 0.12 % Cu were prepared by Q. Xu *et al*. [33], but no clear ferromagnetism was observed. Recently, ferromagnetism in CuO-ZnO multilayers was observed at 300 K, and it depends on the CuO particle size, but not on the CuO-ZnO interfacial area [40].

Finally, magnetic properties related with Cu impurities in GaN were analyzed both theoretically by Wu *et al*. [35] and experimentally by Lee *et al*. [36]. In the latter work, room-temperature ferromagnetism of GaN implanted with Cu was observed after annealing.

1.2.2. Magnetism in organic materials

Ferromagnetism was also observed in several organic materials, which are out of scope of my Thesis, but are mentioned here for the sake of completeness. In particular, experiments demonstrated the presence of ferromagnetic-like features in irradiated pyrolityc graphite [41, 42], or carbon thin films [43], and after implantation of C and N to carbon nanosized particles [44]. Several works reported ferromagnetism in C_{60}-based polymers [45-47]. In particular azafulleren $C_{59}N$, which is formed by replacing a single carbon atom of the C_{60} by a nitrogen atom [48-50] and N-C_{60} molecule [51, 52] have magnetic moments. Ferromagnetism in these systems is weak, since typical Curie temperatures T_C do not exceed 15 K. On the other hand, carbon nano-particles produced by a pulsed arc submerged in ethanol demonstrates a ferromagnetic behavior with a critical temperature much higher than 300 K [53].

Possible origins of FM are local moments at lattice defects or the presence of hydrogen [54]. In particular, theoretical results indicate that FM may be induced by spin moments localized on the dangling bonds of vacancies [55-57]. In proton-irradiated graphite, magnetization increases with the increasing irradiation [42], which can be connected with the increasing concentration of defects [55]. Authors noted that vacancy has spin $\approx 1\ \mu_B$, and spin density is localized on broken bond of carbon. Similarly, the presences of strongly coupled dangling bonds at the edges of carbon nano-ribbons lead to their FM spin polarization [58]. However, it is necessary to stress that the origin of magnetic properties of organic materials are still under debate.

1.2.3. High-spin state of vacancies

Magnetism induced by vacancies was first considered for Ca vacancies in CaO in Ref. [59]. This paper deals with two issues relevant for my Thesis. The first one, discussed above for the impurities, is the fact that sufficiently high concentrations of vacancies in CaO may lead to a FM phase. This issue was examined in Ref. [60], where it was shown that typical concentrations of vacancies are too low to allow for ferromagnetism. However, in a recent paper Peng *et al*. proposes that a high concentration of holes in a ZnO quantum well may mediate the magnetic coupling between the defects and result in FM [61].

The second important issue is the observation that in CaO the Ca vacancy may be in the high-spin state, *i.e*., its spin is higher than 0 or 1/2. The authors show that the effect results

from a strong effective Hund's rule coupling between the electrons that occupy the vacancy-induced states. The first observation of a vacancy in the high-spin state was performed for a neutral gallium vacancy, V_{Ga}, in the irradiated GaP [62]. Analysis of ESR spectra showed that V_{Ga} is in the high-spin S=3/2 state (3 μ_B). The high-spin state of vacancies was also observed in MgO [63, 64], ZnO [65, 66] and in proton-irradiated SiC [67]. In the latter case it was shown that the negatively charged silicon vacancy has a high-spin configuration with spin 3/2. Later, it was shown by L. Torpo *et al*. [68] that in the neutral, singly and doubly negative charge states of V_{Si} in SiC a strong exchange coupling, which prefers parallel electron spin configuration, overcomes the Jahn-Teller energy. In other charge states, the ground state of V_{Si} has a low spin configuration. Subsequent theoretical calculations predicted that neutral cation vacancies in III-N nitrides [69-71] and V_{Zn} in ZnO [61, 69]. Analysis of the results, given in Part 5, demonstrates that the physical origin of two effects that seem to be distinct, *i.e*., the spontaneous magnetization of bulk II-V crystals and the high-spin configuration of vacancies, is the same and consists in the strong spin polarization N and O atoms.

1.3. The plan of Thesis

The basics of methodology, *i.e.*, of the Density Functional Theory (DFT) and of the exchange-correlation functionals in the Local Spin Density Approximation (LSDA) and General Gradient Approximation (GGA), together with the details of calculations, are summarized in Part II. In Part III the electronic, magnetic, and structural properties of several II^A-V compounds are analyzed. I consider four crystal structures: *zb*, *NiAs*, *rs*, and Zn_3P_2. Our results indicate that II^A-V nitrides in the rock salt phase are (meta)stable ferromagnetic half-metals. Part IV is devoted to monoclinic SrN, which is expected to be a molecular antiferromagnet. In Part V, formation and stability of high-spin states of vacancies are analyzed. Cation vacancies in BN, AlN, GaN, GaP, ZnO, BeO were considered. The calculations demonstrated that in these cases the exchange coupling is strong enough to induce high-spin (*i. e.*, spin-polarized) local configurations, which are related with *s* and *p* rather than with *d* atomic orbitals. In contrast, in 'classical' semiconductors like GaAs, V_{Ga} is found in the low-spin state, in agreement with experiment. Part VI summarizes the work.

Part 2

Methodology

The fundamental property of density functional theory (DFT) is that any property of system of many interacting particles can be viewed as a functional of the ground state electron density $n_0(\vec{r})$. In this Part I summarize the methodology of DFT. Section 2.1 describes the Kohn-Sham independent-particle equation in a general form useful for all calculations. Section 2.2 deals with widely used Local Spin Density Approximation (LSDA) and General Gradient Approximation (GGA) for the exchange-correlation functional. Section 2.3 is devoted to the plane wave pseudopotential method, which has been used in our calculation. In Section 2.4 I consider the problem of a choice of the pseudopotentials. In section 2.5 I discuss the details our calculations.

2.1. Density functional theory

The general idea of DFT is that all properties of the ground state of a system can be considered to be functional of the ground state density of particles [72-74].

The Hamiltonian of N electrons in an external potential $V_{ext}(\vec{r})$ can be written as:

$$\hat{H} = -\frac{\hbar^2}{2m}\sum_i^N \nabla_i^2 + \sum_i^N V_{ext}(\vec{r}_i) + \frac{1}{2}\sum_{i\neq j}\frac{e^2}{|\vec{r}_i - \vec{r}_j|}, \qquad (1)$$

where, the first term is a sum operator of kinetic energy of electrons, the second term is a sum of $V_{ext}(\vec{r})$, where in the case of a crystal $V_{ext}(\vec{r}_i) = -\sum_{i\neq j}^{M}\frac{e^2 Z_j}{|\vec{r}_i - \vec{R}_j|}$ is a potential of Coulomb interaction of *i*-electron with nuclei, and the third term is the Coulomb electron-electron interaction.

DFT is based upon two theorems formulated by Hohenberg and Kohn [72].

Theorem 1. The expectation value of any observable is a unique functional of the exact ground state electron density $n_0(\vec{r})$. All ground state properties can thus be extracted from the exact electron density. The problem is now only how to find this density. The second theorem is helpful in this matter.

Theorem 2. For a given external potential, the true density $n_0(\vec{r})$ minimizes the total energy functional. This reduces the very complex problem of finding all physical properties of a system to finding the minimum of the energy with respect to the electron density (which still is not trivial since $n_0(\vec{r})$ is function in three-dimensional space).

Therefore, the total energy of the systems is a functional of electron density and can be written as:

$$E_{tot}^{e}\ [n(\vec{r})] = T[n(\vec{r})] + E_{ext}[n(\vec{r})] + E_{ee}[n(\vec{r})] + E_{xc}[n(\vec{r})], \qquad (2)$$

where $T[n(\vec{r})]$ is the total kinetic energy of a system of non-interacting electrons with density $n(\vec{r})$, $E_{ext}[n(\vec{r})] = \int_V V_{ext}(\vec{r}) n(\vec{r}) d^3r$ describes the electron-nuclei interaction, the so-called Hartree term, $E_{ee}[n(\vec{r})] = e^2/2 \iint_V \frac{n(\vec{r})n(\vec{r}')}{|\vec{r}-\vec{r}'|} d^3r d^3r'$, is the classical energy of the Coulomb electron-electron interaction, and $E_{xc}[n(\vec{r})] = \int_V V_{xc}[\vec{r}, n(\vec{r})] d^3r$ is the exchange-correlation energy functional which compensates for the electron-electron interaction being described only by the Hartree term $E_{ee}[n(\vec{r})]$.

These theorems show is that a unique mapping between the ground state density and the ground state energy in principle exists. However, they do not provide any guidance how the functional that delivers the ground state energy should be constructed. In fact, in (2) only E_{ee} is known, while the explicit forms of the other contributions are unknown. Kohn and Sham invented an ingenious indirect approach to the kinetic-energy functional, which rests on two assumption: [73] (1) the exact ground state density can be represented by ground state density of an auxiliary system of non-interacting electrons, and (2) the Hamiltonian is chosen to have the usual kinetic operator and an effective local potential acting on an electron of spin *s* at point $\vec{r}$.

The density of the auxiliary system is given by sums of squares of the wave function of electrons:

- without spin: $n(\vec{r}) = \sum_{\mu} |\psi_{\mu}(\vec{r})|^2$, (3)
- with spin: $n(\vec{r}) = \sum_{s} n(\vec{r}, s) = \sum_{s} \sum_{\mu} |\psi_{\mu}^{s}(\vec{r})|^2$. (4)

For $E^{e}_{tot}\left[\psi_{\mu}(\vec{r})\right]$ to be a minimum, it is necessary that $\frac{\delta E^{e}_{tot}}{\delta \psi^{*}_{\mu}(\vec{r})}$=0 with leads to the Kohn-Sham equations:

$$\left[-\frac{\hbar^2}{2m}\nabla^2 + V_{ext}(\vec{r}) + e^2\sum_i \int \frac{|\psi_i(\vec{r}')|^2}{|\vec{r}-\vec{r}'|} d^3r' + V_{xc}[\vec{r}, n(\vec{r})]\right]\psi_{\mu}(\vec{r}) = \varepsilon_{\mu}\psi_{\mu}(\vec{r}). \qquad (5)$$

Here ε_{μ} are Lagrange multipliers for the constraints $\int \psi^{*}_{\mu}(\vec{r})\psi_{\nu}(\vec{r})d^3r = \delta_{\mu\nu}$, and are interpreted as one-electron energies. $V_{xc}[\vec{r};n] \equiv \frac{\partial E_{xc}[\vec{r};n]}{\partial n(\vec{r})}$ is the exchange-correlation potential. These equations are nonlinear, self-consistent, and must be solved iteratively. Total energy of the ground state depends on ε_{μ} and the wave function $\psi_{\mu}(\vec{r})$ of the one-electron states:

$$E_{tot} = \sum_{\mu}\varepsilon_{\mu} - \frac{e^2}{2}\int \frac{n(\vec{r})n(\vec{r}')}{|\vec{r}-\vec{r}'|} d^3r d^3r' - \frac{1}{4}\int V_{xc}(\vec{r};n)n(\vec{r})d^3r. \qquad (6)$$

2.2. Local Spin Density Approximation and Generalized Gradient Approximation

In Section 2.1 the Kohn-Sham formalism was introduced what allows for an exact treatment of most of the contributions to the total energy, including the major fraction of the kinetic energy. All remaining and unknown parts are collectively folded into the exchange-correlation functional E_{xc}. In this Section I summarize the commonly used approximate forms of functional for E_{xc}.

Local Density Approximation

The local density approximation (LDA) consist in the assumption that $V_{xc}(\vec{r};n) \cong V^{h}_{xc}(n(\vec{r}))$. Here $V^{h}_{xc}(n(\vec{r}))$ is the exchange-correlation potential of a homogeneous electron gas of density *n*. E_{xc} is the exchange-correlation energy per particle of a uniform electron gas of density *n*. The quantity $E_{xc}[n(\vec{r})]$ can be further split into exchange

and correlation contributions: $E_{xc}[n(\vec{r})] = E_x[n(\vec{r})] + E_c[n(\vec{r})]$. The exchange energy of an electron in a uniform electron gas is [75]: $E_x^h\ [n] = -\frac{3e^2}{4}\left(\frac{3}{\pi}\right)^{1/3} n(\vec{r})^{4/3}$. (7)

The correlation energy of the homogeneous gas was calculated by accurate numerical quantum Monte-Carlo simulations performed by Ceperly and Alder [76]. These results have been fitted by analytic forms for $E_c[n(\vec{r})]$ by Perdew and Zunger [77]. The correlation potential is given as $V_c(r_s) = E_c(r_s) - \frac{r_s dE_c(r_s)}{3dr_s}$, (8)

where the parameter $r_s = (3/4\pi n)^{1/3}$ is the radius of a sphere containing one electron. The expression given in Ref. [77] reads:

$$E_c^{pz}(r_s) = \begin{cases} -0.0480 + 0.031 * \ln(r_s) - 0.0116 r_s + 0.0020 r_s * \ln(r_s), & r_s < 1. \\ -0.1423/(1 + 1.9529 r_s^{1/2} + 0.3334 r_s), & r_s > 1. \end{cases} \quad (9)$$

Generalized Gradient Approximation

The GGA can be formulated in terms of either two spin densities $n^{\uparrow}(\vec{r})$ and $n^{\downarrow}(\vec{r})$, or total density $n(\vec{r})$ and the fractional spin polarization defined as $\xi(\vec{r}) = \frac{n^{\uparrow}(\vec{r}) - n^{\downarrow}(\vec{r})}{n(\vec{r})}$. For unpolarized systems $n^{\uparrow}(\vec{r}) = n^{\downarrow}(\vec{r}) = n(\vec{r})/2$.

The GGA uses not only the density $n(\vec{r})$ at a particular point, but also its gradient $\nabla n(\vec{r})$, in order to account for the non-homogeneity of the true electron density. It is convenient to define the functional in a generalized form [78-80]:

$$E_{xc}^{GGA}[n^{\uparrow}, n^{\downarrow}] = \int d^3 r n(\vec{r}) E_{xc}\left(n^{\uparrow}(\vec{r}), n^{\downarrow}(\vec{r}), |\nabla n^{\uparrow}(\vec{r})|, |\nabla n^{\downarrow}(\vec{r})|, ...\right) \equiv$$
$$\equiv \int d^3 r n(\vec{r}) E_x^h(n(\vec{r})) F_{xc}\left(n^{\uparrow}(\vec{r}), n^{\downarrow}(\vec{r}), |\nabla n^{\uparrow}(\vec{r})|, |\nabla n^{\downarrow}(\vec{r})|, ...\right). \quad (10)$$

Here F_{xc} is function of the density and the density gradient, and $E_x^h[n]$ is given by (7).

The exact exchange energy obeys the spin-scaling relationship:

$E_{xc}[n^{\uparrow}, n^{\downarrow}] = (E_{xc}[2n^{\uparrow}] + E_{xc}[2n^{\downarrow}])/2$.

For exchange one can consider only $F_x(n, |\nabla(n)|)$. Various forms for $F_x(n, s)$ have been proposed, for example by Perdew, Burke, and Enzerhof (PBE) [80], where

$s = \frac{|\nabla n(\vec{r})|}{n^{4/3}(\vec{r})} = \frac{|\nabla r_s|}{2(2\pi/3)^{1/3} r_s}$ is a scaled density gradient. It assumes large values not only for large gradients, but also in regions of small densities, such as the exponential tails far from the nuclei. The form of functional for exchange was proposed in Ref. [80] as $F_x(s) = 1 + k - k/(1 + \mu s^2/k)$, where k = 0.804, and μ =0.21951 is the effective gradient coefficient for exchange, cancels that for correlation. For this form $F_x(s=0) = 1$ and $F_x \to$ *const* at large *s*.

The form for correlation is expressed as the local correlation plus an additive term, both of which depend upon the gradients and the spin polarization:

$$E_c^{PBE}\left[n^{\uparrow}, n^{\downarrow}\right] = \int d^3 r n(\vec{r})\left[E_c^h(r_s, \xi(\vec{r})) + H(r_s, \xi(\vec{r}), t)\right], \qquad (11)$$

where $t = \frac{|\nabla n|}{2\phi k_s n}$ is a dimensionless gradient. Here $\phi = ((1+\xi)^{2/3} + (1-\xi)^{2/3})/2$ is a spin-scaling factor and $k_s = \sqrt{4k_F/\pi a_0}$ is the Thomas-Fermi screening wave number. In Ref. [80] were constructed the gradient contribution as $H(r_s, \xi, t) = \frac{e^2}{a_0}\gamma\phi^3 \log\left(1 + \frac{\beta}{\gamma} t^2 \frac{1 + At^2}{1 + At^2 + A^2 t^4}\right)$. The function A is given by $A = \beta/\gamma[\exp(-E_c^h/\gamma\phi^3 e^2/a_0) - 1]^{-1}$, where β =0.066725, and γ =0.025.

2.3. "Ab-initio" pseudopotentials

In this section I consider the problem of a choice of the potential V_{ext}. Most of physical and chemical properties of crystals depend to a good approximation only on the distribution of the valence electrons. The core electrons do not participate in the chemical bond. They are strongly localized around the nucleus, and their wave functions overlap only very little with the core electrons from neighboring atoms. Thus, one might combine the Hartree potential of the core electrons with the Coulomb potential of the nucleus to an ionic core potential. However, this is not very useful since the valence wave functions still have to maintain their nodal structure in order to be orthogonal to the core states. Thus, the idea of the pseudopotential is the replace of the strong Coulomb potential of the nucleus and the effects of the core electrons by an effective ionic potential acting on the valence electrons.

Pseudopotentials generated based of DFT calculations of atomic-like states are termed "*ab-initio*". The list of requirements for a pseudopotential is given in Ref. [81]. For $r \geq R_{cut}$, where R_{cut} is radius cutoff, one requires that: (i) $\psi(\vec{r}) = \Phi(\vec{r})$ and (ii) $\frac{\partial \psi(\vec{r})}{\partial r} = \frac{\partial \Phi(\vec{r})}{\partial r}$. Here $\psi(\vec{r})$ and $\Phi(\vec{r})$ are the all-electron and pseudo wavefunctions respectively.

It is useful to separate the ionic pseudopotential into a local, i.e. independent, on the angular momentum of electron part of the potential plus non-local (*l*-depended) term:

$$V_{ext}(\vec{r}) = \sum_{i=1}^{M} V_l(\vec{r} - \vec{R}_i) = V_{local}(\vec{r}) + \delta V_{nonlocal,l}(\vec{r}).$$

Since the eigenvalues and orbitals are required to be equal for pseudo and the all-electron case for $r > R_{cut}$, each potential $V_l(\vec{r})$ equals the local all-electron potential, and $V_l(\vec{r}) \to -\frac{Z_{ion}}{r}$ for $r \to \infty$. Thus $\delta V_{nonlocal,l}(\vec{r}) = 0$ for $r > R_{cut}$ and all the long-range effects of the Coulomb potential are included in $V_{local}(\vec{r})$. As it has been shown by Vanderbilt, [82] it is also possible to construct a fully nonlocal potential directly from atomic all–electron calculations. Very difficult to treat within a pseudopotential scheme are all elements with nodeless valence states, in particular those with 2*p* valence electrons for nitrogen. For those elements the pseudo and all-electron wave functions are almost identical. Since these valence electrons are strongly localized in the ionic core region, many plane waves are required for a representation of their wave function which often makes calculations for such elements prohibitively expensive. Vanderbit has introduced ultrasoft pseudopotentials, in which the normconserving requirement has been relaxed [82].

2.4. Plane wave based total energy calculation

In this section the basic expressions for plane wave based total energy calculations are given. Plane waves are especially appropriate for fast Fourier transforms for periodic crystals. In the periodic crystal, the wave functions of electrons are Bloch functions: $\psi_\mu(\vec{r}) = \sum_{\vec{G}} \psi_\mu(\vec{k} + \vec{G}) e^{i\vec{r}(\vec{k}+\vec{G})}$, where $\vec{G}$ is reciprocal lattice vector.

The Kohn-Sham equations can be written as:

$$\sum_{\vec{G}'}\left(\frac{\hbar^2}{2m}\left(\vec{k}+\vec{G}'\right)^2\delta_{\vec{G}\vec{G}'}+V^{\mu}_{\vec{G},G'}\right)\psi_{\mu}\left(\vec{k}+\vec{G}'\right)=\varepsilon_{\mu}\psi_{\mu}\left(\vec{k}+\vec{G}\right). \quad (12)$$

Here $V^{\mu}_{\vec{G},\vec{G}''}=V_{Coul}\left(\vec{G}'-\vec{G}\right)+V_{xc}\left(\vec{G}'-\vec{G}\right)+S\left(\vec{G}'-\vec{G}\right)\left(V_{local}\left(\vec{G}'-\vec{G}\right)+\sum_{l}V_{l,\vec{k}+\vec{G},\vec{k}+\vec{G}'}\right)$, where

$V_{Coul}\left(\vec{G}\right)=\frac{4\pi e^2 n\left(\vec{G}\right)}{G^2}$, $S\left(\vec{G}\right)=\frac{1}{M}\sum_{i=1}^{M}\exp\left(i\vec{G}\vec{R}_i\right)$ is the structure factor for each species $\vec{k}$, thus

$V_{Coul}\left(\vec{G}=0\right)=0$, $V_{local}\left(\vec{G}=0\right)=0$, $S\left(\vec{G}=0\right)=1$. $V_{xc}(\vec{G}'-\vec{G})=V_{xc}(\vec{G})n(\vec{G})$;

$V_{l,\vec{k}+\vec{G},\vec{k}+\vec{G}'}\equiv\frac{4M\pi}{V}(2l+1)\int V_l(\vec{r})j_l\left(\left|\vec{k}+\vec{G}\right|\vec{r}\right)j_l\left(\left|\vec{k}+\vec{G}'\right|\vec{r}\right)r^2 d\vec{r}P_l\left(\cos(\gamma)\right)$, where *V*- is volume of unit cell, $j_l\left(\vec{k}+\vec{G}\right)$ are spherical Bessel functions, $P_l\left(\cos(\gamma)\right)=P_l\{[\vec{k}+\vec{G}][\vec{k}+\vec{G}']/[|\vec{k}+\vec{G}|][|\vec{k}+\vec{G}'|]\}$ are the Legendre's polynomials. Thus:

$$E_{tot}=\sum_{\mu}\varepsilon_{\mu}-\frac{V}{M}\left(\frac{1}{2}\sum_{\vec{G}}V_{Coul}\left(\vec{G}\right)n\left(\vec{G}\right)+\sum_{\vec{G}}E_{xc}\left(\vec{G}\right)\right)+\frac{V}{M}\lim_{\vec{G}\to 0}\left(\frac{1}{2}V_{Coul}\left(\vec{G}\right)n\left(\vec{G}\right)+V_{local}\left(\vec{G}\right)n\left(\vec{G}\right)\right)$$

2.5. Details of calculations

In our calculations the exchange and correlation effects have been treated using both the generalized gradient PBE [80] and the local spin density PZ [77] approximations. Most of the calculations were performed within GGA, which typically is more accurate for magnetic systems. Test LSDA calculations were performed for several cases, and quantitatively similar results were obtained using the two approximations for both structural parameters and spin polarization energies. I have employed ESPRESSO code [83], and ultrasoft atomic pseudopotentials [82]. The orbitals that were chosen as valence orbitals for pseudopotentials: Be- 2*s*, 2*p*, Mg-3*s*, 3*p*, Ca-3*s*, 3*p*, 4*s*, 3*d*, Sr-4*s*, 4*p*, 4*d*, 5*s*, 5*p*, Ba-5*s*, 5*p*, 5*d*, 6*s*, 6*p*, N-2*s*, 2*p*, P-3*s*, 3*p*, As-4*s*, 4*p*, Sb-5*s*, 5*p*, B-2s, 2*p*, Al-3*s*, 3*p*, Ga-3*d*, 4*s*, 4*p*, C-2*s*, 2*p*, Si-3*s*, 3*p*, Zn-3*d*, 4*s*, and O-2*s*, *2p*. I also used the plane wave basis with the kinetic energy cutoff of 35 Ry ($\frac{1}{2}\left|\vec{G}+k\right|^2\le E_{cut}$). Brillouin zone integrations were performed using a regular mesh of (12×12×12) *k*-points for *zb* and *rs* structures, and equivalent meshes for other structures. The general expression for *k*-point mesh proposed by Monkhorst and Pack is $\vec{k}_{n_1,n_2,n_3}\equiv\sum_{i}^{3}\frac{2n_i-N_i-1}{2N_i}\vec{G}_i$, where $\vec{G}_i$ are the primitive vectors of the reciprocal lattice [84].

The relaxation of atomic positions was performed until the forces acting in atoms were smaller than 0.01 eV/Å. The convergence with respect to E_{cut} and k-point sampling was tested.

In the Part V I used the supercell approximation method. In the supercell approximation one repeats periodically a finite unite cell containing the desired defect plus neighboring host atoms. In the calculations it is important that extended states of the defect are represented well. This can be obtained if the size and shape of the supercell are appropriate. A good description of defect states requires that the interaction between periodically repeated defects is weak. Otherwise, if the defect-defect distance is not large enough, the electronic structure of the defect is distorted because the levels in the band gap form energy bands with a finite dispersion. The small size of the supercell can also restrict the atomic relaxations around the defect. For these reasons in our calculation the large periodic supercell with 64, 216 or 512 atoms for *zb* structure, and with supercell containing 72 or 128 atoms for *w* structure were used. Calculations for the supercells have been done using 2×2×2 Monckhorst- Pack k-mesh for vacancies in 64, 72, 128, 216-atom supercells, and Γ-point for 512-atom supercells. The calculations showed that the appropriated results only in 128 and 512- atom supercell take place, except *zb*-GaP, it is appropriates in 216 – atom supercell.

Part 3
Magnetism of II^A-V compounds

As it was summarized in Part 1, several II^A-V group materials are predicted to be half-metals with a total spin polarization of holes in the valence band [1-4]. In this Part I analyze in detail stability of the ferromagnetic phase of bulk II^A-V materials for various crystal structures. In fact, in contrast to III-V or II-VI compounds that typically crystallize in the *zb* structure, II-V compounds crystallize in variety of structures [7-11, 85-97]. Consequently, I consider here four structures: zinc blende (*zb*), rock salt (*rs*), *NiAs*, and Zn_3P_2. A detailed analysis is performed for the most interesting *rs* phase, since according to the obtained results the *rs*-II^A-V nitrides are FM. Finally, I identify the mechanism of stabilization of spin polarization in both the *rs*- and *zb*-II^A-V nitrides.

3.1. Magnetic properties and electronic structure of II^A-V compounds

In this Section, I analyze the magnetic structure of a number of II^A-V compounds, namely: MgP, MgAs, CaN, CaP, CaAs, CaSb, SrN, SrP, SrAs, BaN, and BaAs. The analysis is based on the calculation of the total energies, magnetic moments, charge densities, spin densities, and density of states (DOS) of these compounds. The value of the lattice parameter *a* corresponding to the minimum of total energy is the equilibrium lattice constant a_{eq} of the given phase. For the hexagonal structure, the lattice constants are obtained by minimizing the total energy with respect to both a, c/*a* and the internal displacement parameter. I begin with *zb*-CaP as example. Total energies of ferromagnetic (spinpolarized) FM and paramagnetic (unpolarized) PM phases as functions of lattice constant are shown in Fig. 3.1. It is found that the FM state is the ground state of *zb*-CaP.

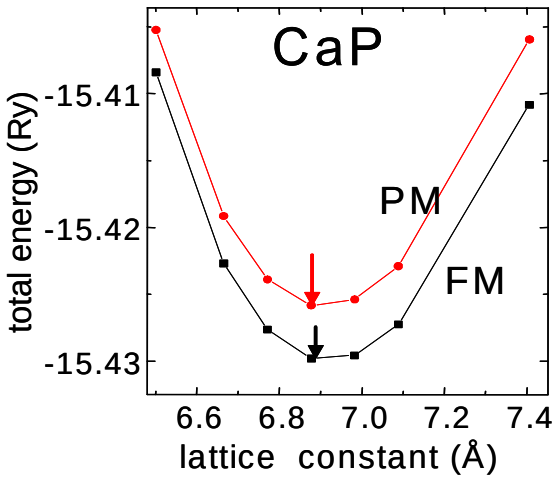

Fig. 3.1. Dependence of the total energy on the lattice constant value of non magnetic (PM) and ferromagnetic (FM) phases for zb-CaP. Arrows indicate the equilibrium lattice constants a_{eq}.

Table 3.1. Energies of spin polarization $\Delta E^{\text{FM-PM}}$ and $\Delta E^{\text{FM-AFM}}$ (in meV per 2 atoms) for *rs*, *NiAs*, and *zb* structures, (in meV per 2 atoms). Last column gives energies of spin polarization of isolated group-V atoms (in eV).

	$\Delta E^{\text{FM-PM}}$ (crystal)			$\Delta E^{\text{FM-AFM}}$ (crystal)		$\Delta E^{\text{FM-PM}}$ (anion)
	rs	*NiAs*	*zb*	*rs*	*zb*	
BaN	–90	–105	–125	–5	–45	
SrN	–135	–205	–185	–35	–50	
CaN	–140	–125	–195	–65	–50	–2.45
CaP	–3	0	–55	0		–1.37
CaAs	0	0	–40			–1.24
CaSb	0	0	–5			–1.02

The stability of the spin-polarized (FM) case relative to the non-polarized (PM) situation is given by the energy difference $\Delta E^{\text{FM-PM}} = E^{FM}\text{-}E^{PM}$. We also calculated the difference in energies of FM and antiferromagnetic of I type (AFM) phases, $\Delta E^{\text{FM-AFM}}$. The calculated magnetic properties of the considered compounds at equilibrium are summarized in Table 3.1.

First, one can see that the spin polarization of the considered compounds in the *zb* structure is non-vanishing. This result holds for SrAs and BaAs as well. The smallest values are fared for *zb*- MgN ($\Delta E^{\text{FM-PM}}$ = -6 meV). On the other hand, *zb*-MgP, *zb*-MgAs, and all *zb*-Be-V [3] crystals are paramagnetic, *i.e.* $\Delta E^{\text{FM-PM}} = 0$. Second, the energy of spin polarization increased with a decrease of atomic number of an element of group II^{A} (a cation). For example, $\Delta E^{\text{FM-PM}}$ is -125, -185, and -195 meV for BaN, SrN, and CaN, respectively. For Ca-V materials $\Delta E^{\text{FM-PM}}$ increased with the decrease of atomic number of an element of anion. So, $\Delta E^{\text{FM-PM}}$ is -5, -40, -55, and -195 meV for CaSb, CaAs, CaP, and CaN, respectively. In more details we shall consider it in the Section 3.1.2. Next, as it follows from the Table 3.1, in both the *rs* and the *NiAs* structure only the II^{A}-nitrides are FM. Regarding $\Delta E^{\text{FM-PM}}$ as a rough estimate of the Curie temperature we observe that $\Delta E^{\text{FM-PM}}$ of about 100 meV corresponds to about 1000 K. Consequently, one may expect II^{A}-nitrides in *rs* phase to be FM at temperatures of the order of 100 K.

Finally, independent of the crystal structure, the calculated magnetic moment per two atoms μ is always equal to 1 μ_B in the spin polarized phase. A borderline case is *rs*-CaP, for which the very small $\Delta E^{\text{FM-PM}}$ = -3 meV is practically vanishing within our numerical accuracy, consistently with its small magnetic moment, 0.2 μ_B. In contrast, Ca_3N_2, Sr_3N_2, Ba_3N_2 in the Zn_3P_2 structure are paramagnetic.

I have also investigated the relative stability of FM and AFM phases. The calculations were performed only for the most interesting cases of *rs* and *zb* phases of II^{A}-N nitrides. (This is because the *NiAs* structure is less stable than *rs*, see Section 3.2, and spin polarization of other *rs*-II^{A}-V crystals vanishes.). To this end I considered the type-I AFM ordering, in which spins of anions in every (001) plane are parallel, but the sign of the polarization of consecutive planes alternates [98]. The calculated differences between energies of FM and AFM phases, $\Delta E^{\text{FM-AFM}}$, are given in Table 3.1. The results show that in all crystals the FM phase is the ground state magnetic order. Furthermore, the absolute values of energy of spin polarization ($\Delta E^{\text{FM-PM}}$) are higher than those of $\Delta E^{\text{FM-AFM}}$. This shows that with the increasing temperature spin polarization should vanish as a result of the disordering of the magnetic moments, and not of their disappearance. Like with the $\Delta E^{\text{FM-PM}}$ energy $\Delta E^{\text{FM-AFM}}$ increases with the decreasing atomic number of the cation: $\Delta E^{\text{FM-AFM}}$ is -5, -35, and -65 meV for BaN, SrN, and CaN, respectively.

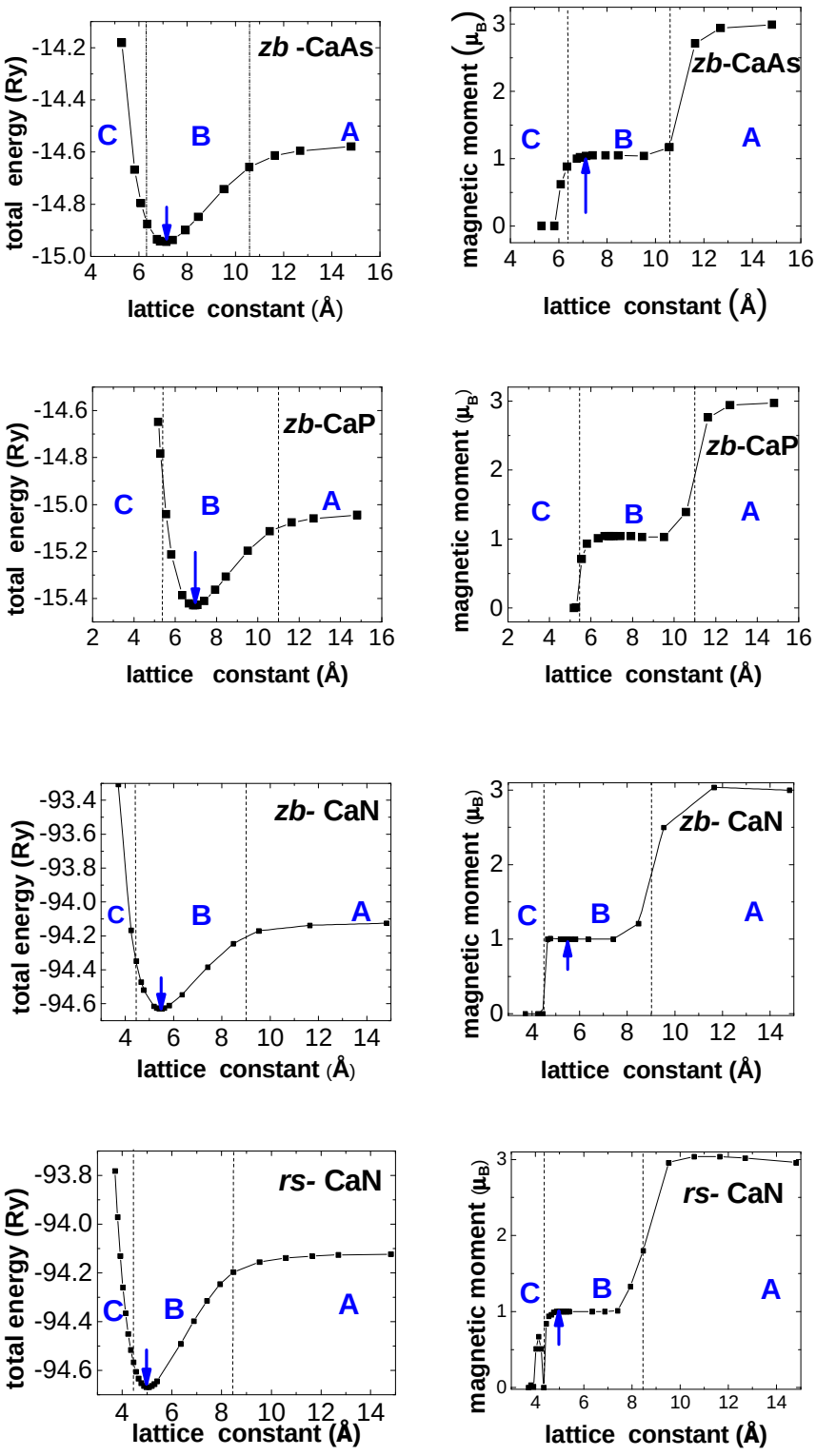

Fig. 3.2. Total energy and total magnetic moment per unit cell as function of the lattice constant of CaAs, CaP, and CaN. Arrows indicate the equilibrium lattice constants a_{eq}.

In order to understand the calculated magnetic properties we will follow the formation of an II^A-V crystal beginning from the case of isolated atoms, and ending with the case of a compressed solid. The calculated total energies and the magnetic moments of *zb-CaAs*, CaP, CaN, and *rs*- CaN are shown in Fig. 3.2. These results are typical for all the considered II^A-V crystals. One may see that there are three ranges of lattice constants characterized by qualitatively different properties, for which the magnetic moment per unit cell is 3, 1, and 0 μ_B, and denoted as A, B, and C, respectively.

3.1.1. Hund's rule. Magnetic moments of isolated atoms

I shall now discuss the obtained results beginning with the case of large lattice constants, *i. e.*, region A in Fig. 3.2. This case corresponds to the situation of "isolated" atoms. The "band structure" of CaAs at 15 Å is show in Fig. 3.3. From Fig. 3.3 one can see that in this case band are not formed. The total energy of this "compound" is the superposition of atomic energies of cation and anion. Similarly, the total magnetic moment is the superposition of magnetic moment of Ca and As. The total magnetic moment per cell is 3 μ_B. This stems from the fact that Ca (and other group- II^A atoms) has 2 valence electrons with opposite spins on the *s* orbital, and its magnetic moment vanishes, while N (and other group-V atoms) has 5 valence electrons, three of them from the *p* orbital have parallel spins according to Hund's rule, and the magnetic moment of N is 3 μ_B (Fig. 3.3).

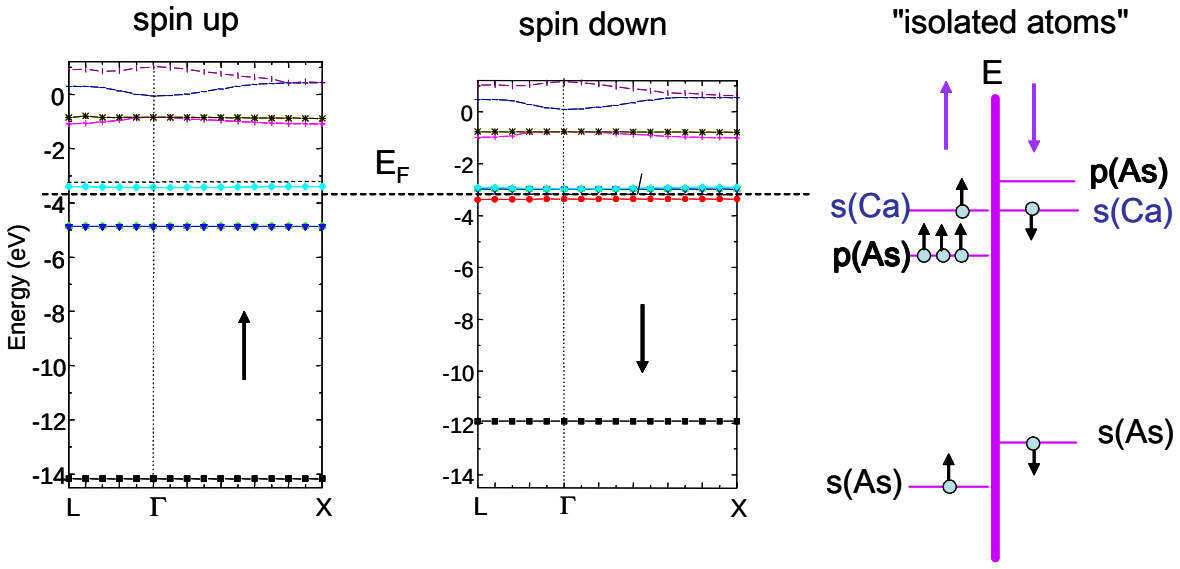

Fig. 3.3. "Band structure" and the electronic levels scheme of CaAs at a = 15 Å.

By the same arguments, magnetic moment of GaAs (Fig. 3.15) is 4 μ_B per unit cell (when the spins of Ga and As are parallel).

It is known that spin moments of electrons in an atom or an ion give rise to their magnetic properties. The relative orientations of spins are determined by the interactions between the electrons together with the Pauli exclusion requirement. In the ground state the electronic configuration of an atom is determined by the first Hund's rule. In our calculations we neglect the spin-orbit interactions, and thus, the third Hund's rule does not apply. Below, briefly summarize the physical interpretation of the first Hund's rule because the spin polarization energy obtained in calculations by LSDA (or GGA) is equivalent of Hund's first rule energy.

The first Hund's rule asserts that, within a given configuration of one-electron orbitals, the ground state of isolated atom has largest value of the total spin. A reason for the increased stability of high multiplicity states is that the different occupied spatial orbitals create a larger average distance between electrons, reducing electron-electron repulsion energy. It has been shown that the actual reason behind the increased stability is a decrease in the screening of electron-nuclear attractions. To understand the effect of the exchange (spin-spin) interaction usually considers as example an atom of carbon, *i.e.*, the case of two electrons on *p*-orbitals. In this case, the state with spins in parallel (triplet) state lower in the energy than the state with spins in antiparallel (singlet) state. The fact that the spins are parallel makes the spin part of the wavefunction to be symmetric, and forces the spatial part to be antisymmetric. An antisymmetric spatial wavefunction for two electrons implies a larger average distance between them than a symmetric function. The electron location probability is squared wavefunction, and the squared antisymmetric function vanishing when $|r_1-r_2|= 0$. This is called the exchange hole effect [99]. In general, probability for a small separation between two electrons is smaller for a symmetric spatial wavefunction than for the antisymmetric one. In parallel, a second effect takes place: if electrons are on average further from each other, then there will be less shielding of the nucleus for another electron, so a given electron will therefore be more exposed to the nucleus. This implies that it is more tightly bounded and lowers in energy. In short, *p* electrons if, e.g., As have the same kinetic energy, and the same potential energy of the nucleus. Parallel-spin electrons avoid each other more effectively because the exchange hole effect takes place and increase the attraction by the nucleus. Hund's first rule follows.

So, when there is choice of putting either two unpaired electrons in two different degenerate orbitals of *p* subshells, or two paired electrons in the same orbital, Hund's rule indicates that the former arrangement is of lower energy. For example, if there are three available *p* orbitals (p^x, p^y, p^z) the first three electrons will fill these one at a time, each with the same spin. When the fourth electron is added, it will enter the p^x orbital and will adopt the opposite spin since this is a lower energy configuration.

3.1.2. Energy bands and magnetic moments at equilibrium

With the decreasing lattice constant the atoms begin to interact and form bonds. This leads to a decrease of the total energy and to a drop of the magnetic moment from 3 to 1 μ_B. Fig. 3.2 shows that the onset of formation of bonds (displayed by the decrease of the total energy) is correlated with the drop of magnetization, which occurs at ~9 Å for *zb*-CaN, and ~8.5 Å for *rs*-CaN. The magnetic moment is then constant for 4.5 Å < *a* < 9 Å for the *zb*, or 3.7 Å < *a* < 8.5 Å for the *rs* phase, respectively. The drop of the magnetic moment is due to the changes in the electronic structure and charge transfer effects induced by formation of bonds. A detailed analysis of the electronic structure is presented below.

Atomic origin of spin polarization

I begin with the most important question, which is the origin of the ferromagnetism found for several II^A-V crystals. I identify it by analyzing their electronic structure. The emerging picture is particularly clear for the zinc blende phase. Considering the series of Ca compounds (CaN, CaP, CaAs, CaSb) one can see from Table 3.1 that $\Delta E^{FM\text{-}PM}$ is the largest for CaN, −195 meV, it decreases with the increasing atomic number of the anion, and it almost vanishes for CaSb. This suggests that anions play a dominant role in determining the spin polarization of crystals. In fact, as it clearly follows from Fig. 3.4, this trend found for crystals is in full agreement with the trend exhibited by the calculated energies of spin polarization of isolated anions, which decrease from −2.45 eV for N to −1.02 eV for Sb. Moreover, the spin polarization energy is about twice higher for N than for the remaining anions. This fact explains not only the presence of the FM order in *zb* SrN and BaN, but also the pronounced stabilization of spin polarization found for both the *NiAs* and the *rs* structures

of the nitrides, see Table 3.1. This result suggests that the driving force of ferromagnetism of II^{A}-V compounds is the spin polarization of partially occupied *p*(anion) orbitals.

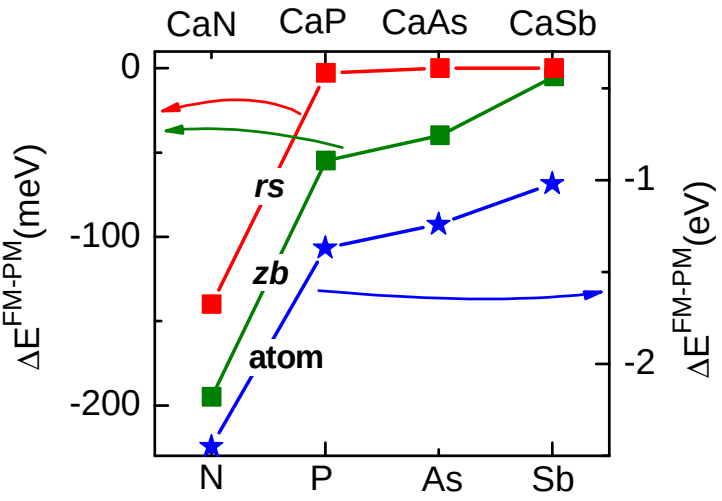

Fig. 3.4. Difference in energies of FM and PM phases ΔE^{FM-PM} for CaX compounds in the rs and zb structures, together with those for isolated anions. The lines are to guide the eye.

This hypothesis is confirmed by the analysis of the density of states (DOS) and of projection of the wave function on atomic orbitals shown in Figs. 3.5 -3.8 for *zb*-CaN, CaAs and SrN, CaN, CaP, and CaAs in the *rs* structure.

Fig. 3.5 shows the calculated spin-resolved total and partial densities of states (DOSs) of *zb*-CaN at its equilibrium lattice constant. We see that the states of majority-spin electrons on Fermi level are filled. These states are formed mainly by the 3(*p)* N states with a very small contribution (< 8 %) from Ca states. For the minority-spin chancel, the states on Fermi level also originate mainly from the 3*p*(N) states, but in this case the Fermi level crosses the bands. The lowest valence states (<-6 eV) for both up and down spin channels are formed by the 3*s*(N) states, and the conduction bands in both spin channels are mainly of *4d*(Ca) character. The very small contribution (< 0.6 %) from *5s*(Ca) states to valence and conduction bands.

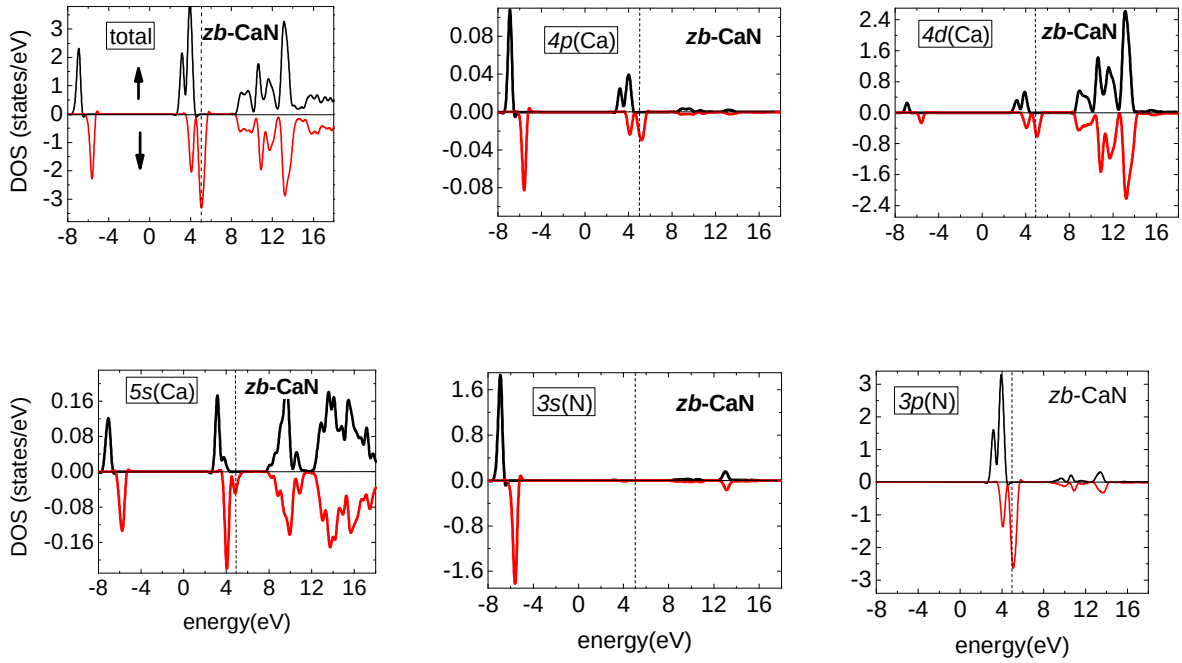

Fig. 3.5. Density of states per unit cell of zb-CaN. Both the total DOS and the contributions of p and d orbitals are given. Vertical lines show the Fermi energy. Positive and negative values of DOS hold for spin-up and spin-down states, respectively.

Very similar results are obtained for the *zb* phase of all II^A-V compounds in spite of differences in the detailed dispersions of energy bands.

In all considered *rs*-II^A-V compounds (see Fig. 3.6) the top of the valence band also is mainly formed from the *p* orbitals of anions, which contribute about 75 per cent. The contribution of *d* orbitals of cations to the valence bands is at least five times smaller. These orbitals (which are the lowest excited states of cations) contribute mainly to the higher conduction states. In particular, they give rise to a *d*(Ca)-derived bands at about 4-8 eV above the bottom of the conduction band. The spin polarization of SrN and CaN is visible; one may also see a very weak polarization in CaP, while that of CaAs vanishes.

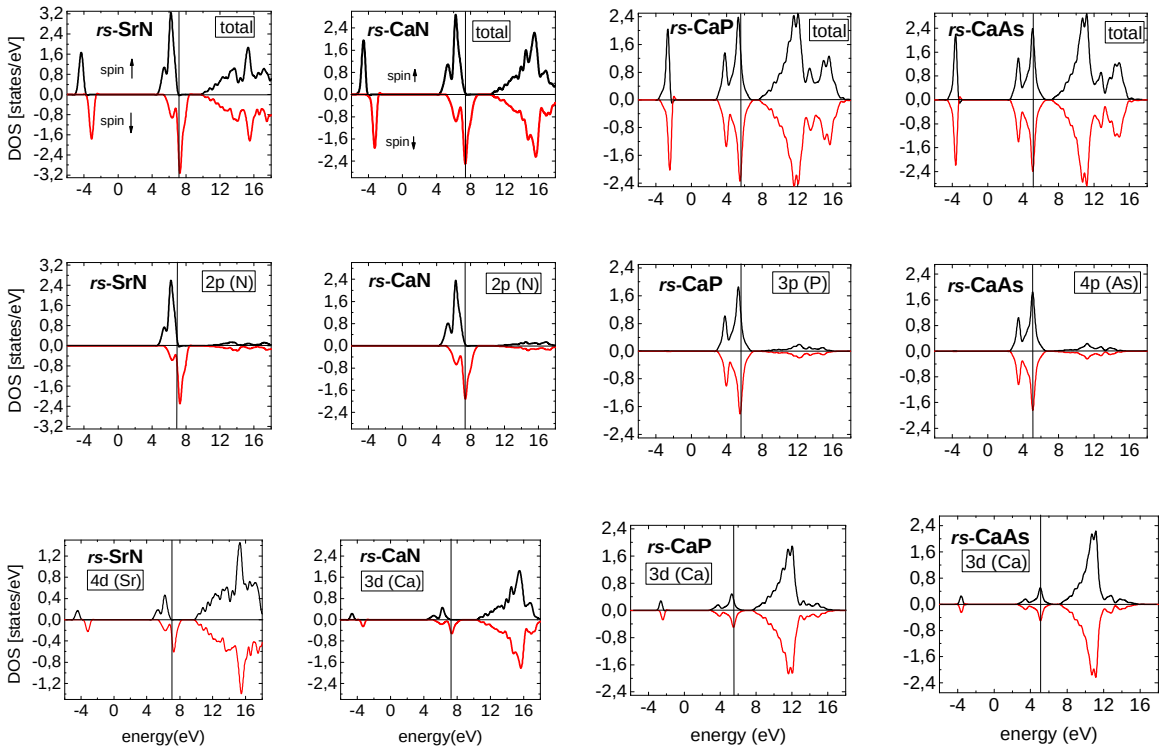

Fig. 3.6. Density of states per unit cell of SrN, CaN, CaP, and CaAs in the rs structure. Both the total DOS and the contributions of p and d orbitals are given.

Figs. 3.7 and 3.8 confirm the conclusion that the spin polarization of crystals results from the spin polarization of the *p*(anion) states. A plot of the charge and spin density of CaAs is shown in Fig. 3.8. One can see that the spin density is well localized at the As site. From the plot of charge density can see that the charge density is strong localized at the atoms and it's the spherical form. Therefore, *zb*-CaAs is ionic compounds. Quite probably, that ionicity of the compound plays an important role for magnetism.

The contour plot of the spin density displayed in Fig. 3.8 for both *zb* and *rs*-CaN also shows that the spin polarization is strongly localized in the vicinity of N atoms. In accord with Fig. 3.7, the contribution of Ca states is visible, but small. Qualitatively identical results are obtained for BaN and SrN. Finally, we note that a large contribution of the *d*(Ca) states to the valence bands could in principle explain the magnetism of II-V compounds, which would then have an origin similar to that in systems containing transition metal atoms. This explanation was suggested by Kukasabe *et al*. [1]. However, the obtained results show that this is not the case.

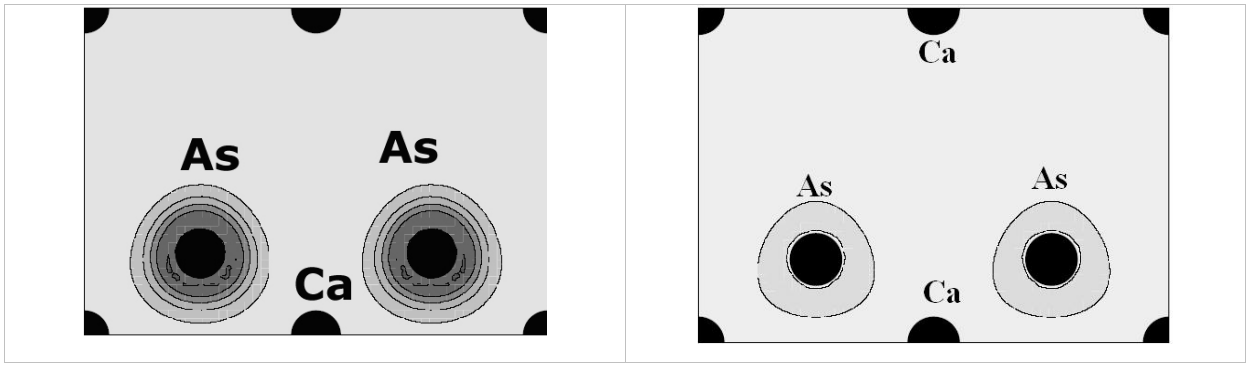

Fig. 3.7. Contour plots of the calculated charge (left panel) and spin (right panel) densities for zb-CaAs in the (110) plane.

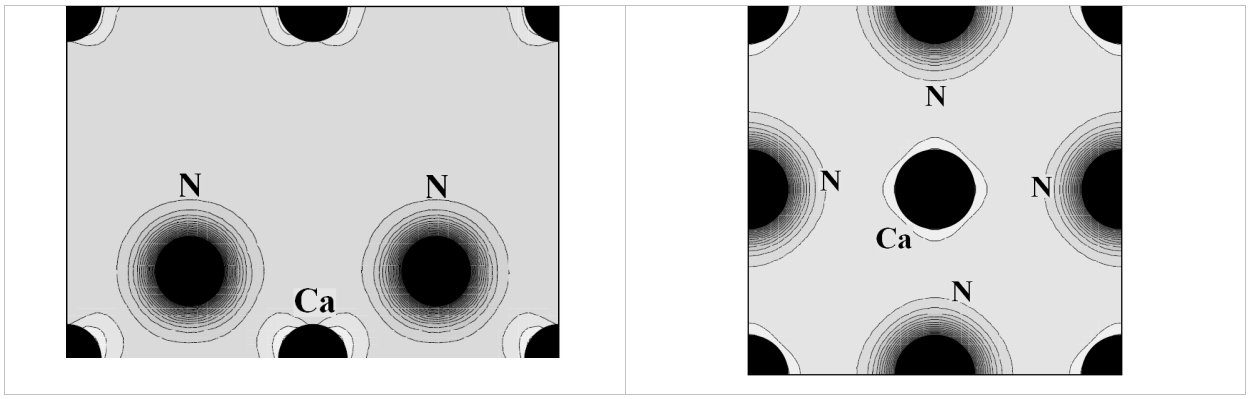

Fig. 3.8. Contour plots of the calculated spin density for zb-CaN in the (110) plane (left panel), and rs-CaN in the (001) plane (right panel).

Energy bands and magnetic moments at equilibrium

The spin-polarized band structures of ferromagnetic *zb*-Ca-V compounds at equilibrium lattice constants are shown in Fig. 3.9. Figure 3.10 shows the band structure of the *NiAs*-CaN. And finally the calculated band structures of CaN, CaP, CaAs, SrN, and BaN in the *rs* phase at equilibrium are shown in Fig. 3.11 (energy bands of CaSb are similar to these of CaAs).

With the decreasing lattice constant from the case A of isolated atoms to the case B, the electrons begin to form chemical bonds. In particular, for CaN the bonding combination of *p*(N) with Ca orbitals decreases in energy and forms the Γ_{15} top of the valence bands, while the antibonding combination of *s*(Ca) with *s*(N) and *p*(N) orbitals rises in energy and forms

the bottom of the conduction band, see Figs. 3.9-3.11. Consequently, 2 electrons are transferred form *s*(Ca)-derived to spin-down *p*(N)-derived states, reducing the magnetic moment from 3 to 1.

I begin with an analysis of the band structure of *zb* phase (see Fig. 3.9). In all cases, in these materials two spin bands show a completely different behavior. While the minority spin band (referred to as spin-down band) electrons exhibit metallic character, the majority-spin (referred to as spin-up band) channel exhibits a semiconducting behavior with an energy gap at the Fermi level. Therefore *zb*-II^{A}-V compounds are half-metals with the full spin polarization of holes in Fermi level. For CaSb both the spin up and spin down electrons show metallic character. This is the reason for which the energy of spin polarization is small (-5 meV) in this case.

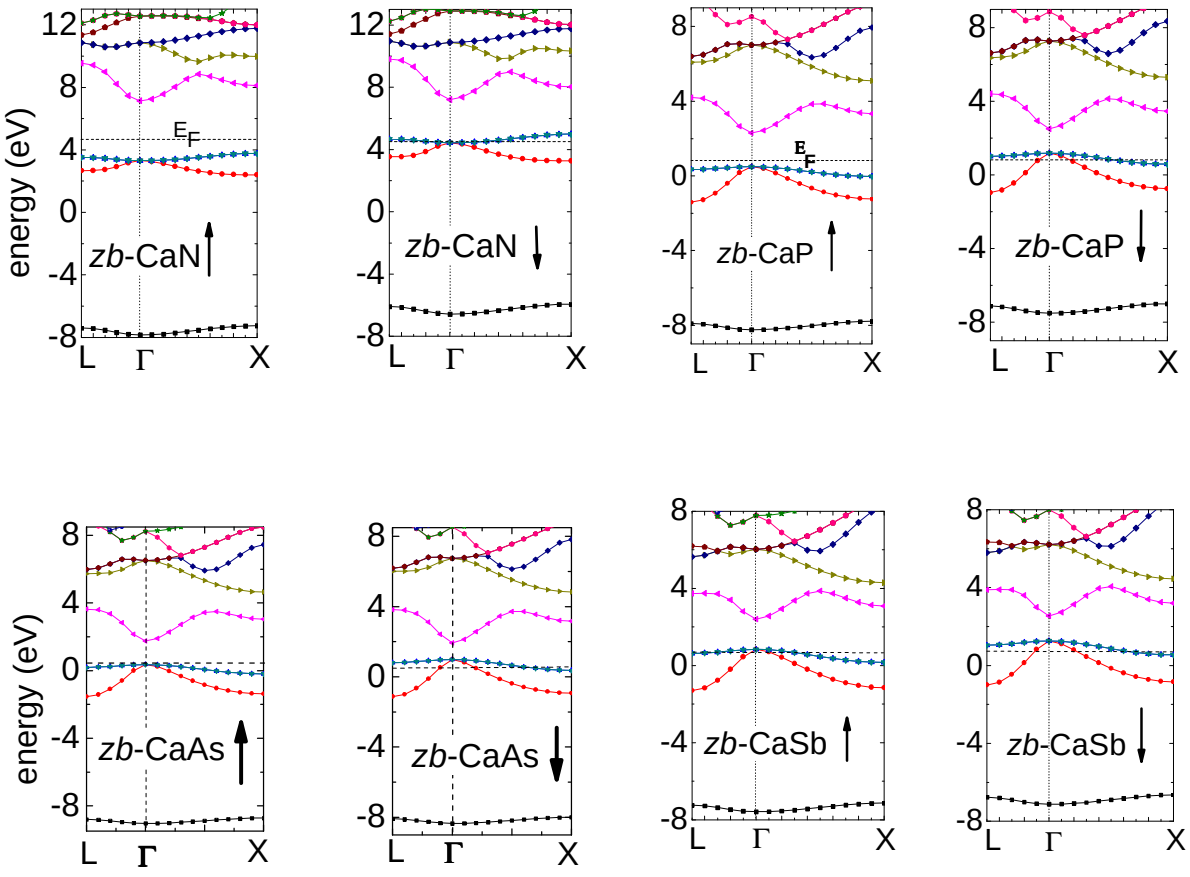

Fig. 3.9. Band structures of zb-CaN, CaP, CaAs, and CaSb at equilibrium.

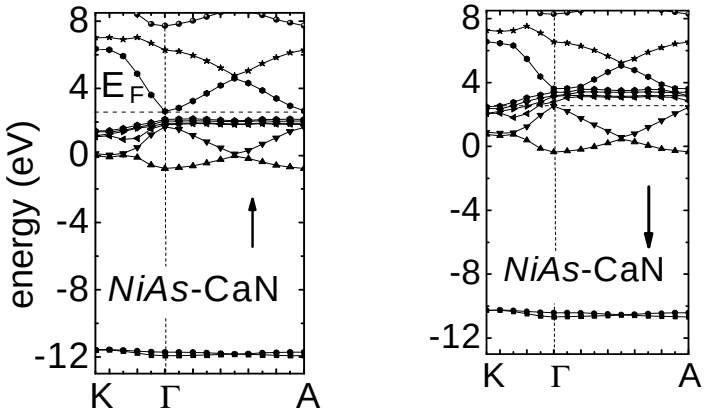

Fig. 3.10. Band structure of NiAs-CaN at equilibrium for spin-up and spin-down states.

I now turn to the *NiAs* structure (see Fig. 3.10). Below we find that this phase is more stable than *zb* for all the considered compounds. However, from the Table 3.1 it follows that in the *NiAs* structure only II^A-nitrides are ferromagnetic at equilibrium. The typical complex band structure of *NiAs*-CaN is shown in Fig. 3.10; we see that the system is a half-metal.

Figure 3.11 shows that energy bands of *rs*-II-V compounds compared with those of typical III-V or II-VI crystals in the *zb* phase exhibit characteristic differences:

(i) II-V crystals have 7 valence electrons per unit cell, and thus they are not insulators but metals with one free hole per cell.

(ii) In all FM II-V nitrides, the free hole gas is fully spin-polarized, and therefore these crystals at equilibrium are half-metals. As it was mentioned above, in CaP spin polarization is very small. Finally, in CaAs the holes are not spin-polarized, and this compound is a paramagnetic metal.

(iii) The valence bands of CaN, CaP, and CaAs are similar in shape to these of, *e.g.*, a typical III-V compound GaAs. On the other hand, the structure of the conduction bands is different. In particular, there are additional bands that originate in the 3*d*(Ca) orbitals, which also are seen in Fig. 3.7. Moreover, the bottom of the conduction band occurs at the *X* point of the Brillouin zone.

(iv) Turning to the series CaN, SrN, and BaN we observe an interesting trend consisting in the change of relative energies at the Γ and *X* points. Namely, in CaN the

curvature of the highest valence bands along the Γ-*X* direction is small, but the maximum of this band occurs at Γ. In the case of both SrN and BaN, the band maximum is shifted from Γ to *X*. Consequently, in these two compounds the gap has a direct character, but the gap minimum occurs at the *X* point. Moreover, the minimum of the lower valence band situated about 10-12 eV below the top of the valence band is shifted from Γ to *X*. The small dispersions and atypical shapes of the valence bands result mainly from the large values of the lattice constant due to the large atomic radii of the heavy Ca, Sr, and Ba cations. Moreover, since the top of valence band is mainly formed from *p*(N) orbitals that have a small atomic radius, the overlap between cations, *i. e.*, second neighbors, may play an important role in determining the actual dispersion of these bands.

According to the obtained results, *rs*-II-N nitrides are half-metals. Nevertheless, the flatness of the upper valence band may suggest that these systems are magnetic Mott-Hubbard insulators, similarly to several transition metal oxides in which strong electron correlations play a critical role. This possibility may be verified by calculations beyond LSDA that use methods appropriate for highly correlated systems. However, even if this would be the case, the main physical effect on which we focus here, *i. e.*, the magnetism based on partially filled *p* (and not *d* or *f*) atomic shell, would remain valid.

Finally, the band structure of II^A-V compounds in Zn_3P_2 phase is complex and 'obscure' due to the fact that the unit cell contains 40 atoms with 128 valence electrons, which occupy 64 bands spanning an energy range of about 10 eV. For this reason we do not show it. The most important result that should be pointed out is that Ca_3N_2, Sr_3N_2, and Ba_3N_2 are all insulators with the calculated band gaps of about 0.5 eV. The insulating character of these compounds follows in particular from the fact that there is an even number of electrons per unit cell. Consequently, there are no free holes and the spin polarization is zero

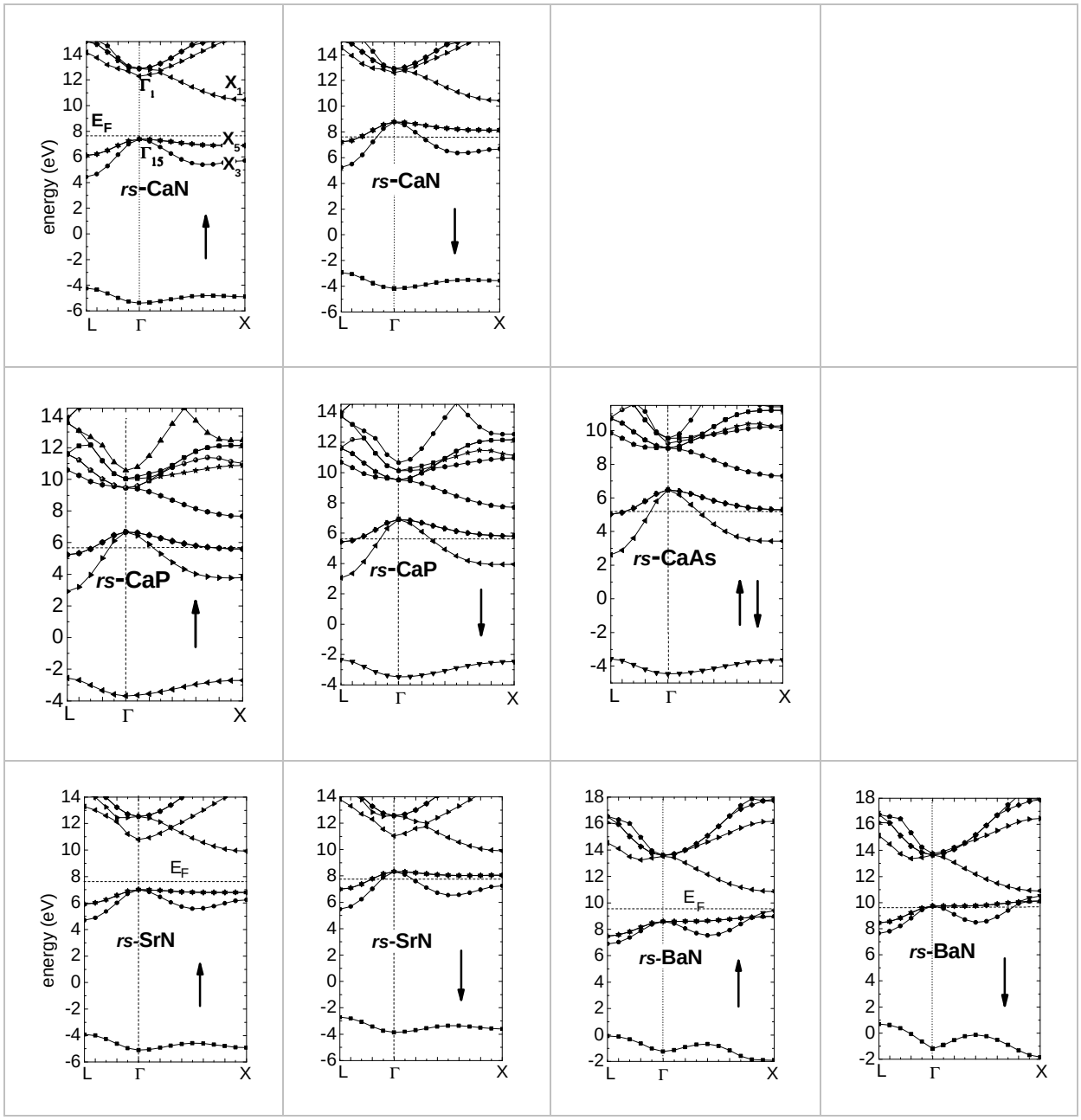

Fig. 3.11. Band structures of rs-CaN, CaP, CaAs, SrN and BaN at equilibrium.

3.1.3. Electronic structure at high pressures

I now turn to the FM-to-PM transition, *i. e.*, to the destabilization of the spin polarization that occurs at sufficiently small lattice constants for all the considered compounds. This transition is seen in Fig. 3.2 for II^{A}-V compounds (the region C). In all cases, the disappearance of the magnetization is not accompanied with major and abrupt

changes of the band structure, and the decreasing lattice constant induces a progressive decrease of the spin splitting, as well as an increase of the width of the valence bands. In this Section we point out that independently of the actual origin of spin polarization, the kinetic energy and its increase with the decreasing atomic volume under hydrostatic pressure always play an important role in destabilizing the FM phase. The pressure-induced disappearance of the spin polarization may qualitatively be understood based on the Stoner criterion [100]. This criterion indicates that the stability of spin polarization is favored by large magnetic susceptibility, which is proportional the density of states at the Fermi level, and is destabilized by kinetic energy E_{kin} at high electron densities. We briefly discuss these factors.

Previously, the dependence of the magnetic ordering on the external pressure (which is equivalent to the change of the lattice constant, or the change of the electron density) has been considered for two types of systems. The first one is the model case of free electron gas, analyzed within both the Hartree-Fock approximation, and by extensive quantum Monte Carlo calculations [76,101,102]. Second, the FM-to-PM transition induced by the increasing hydrostatic pressure has been observed for a number of real compounds containing transition metals, such as MnN. In both cases, the origin of spin polarization and the mechanism of transition to the paramagnetic phase are different. Below, we discuss both cases, and show that II-V do not belong to either case.

In the case of MnN, both the origin of magnetism and the reason of its disappearance at high pressures are different. Magnetism is due to the presence of transition metal Mn ions, which have a non-vanishing spin moment. However, at high pressures the crystal field splitting of the half-filled *d*(Mn) shell exceeds the exchange splitting onto *e* doublet and t_2 triplet states, which induces transfer of electrons from the spin-up t_2 states to the spin-down e states, reducing the magnetic moment to zero [97].

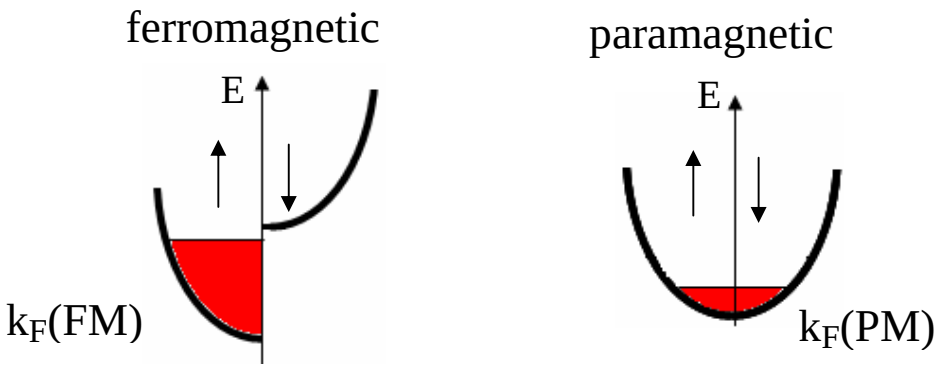

Fig. 3.12. Electronic level scheme for the FM and PM states.

I now turn to the case of free electrons. Within the Hartree-Fock approximation, free electrons at sufficiently low electron densities are spin polarized due to the exchange coupling. Magnetic properties of free electrons have been analyzed in a much more exact way by quantum Monte Carlo calculations [76, 102], which include electronic correlations. It was found that the FM phase induced by the exchange interaction is stable in the density range $6\times10^{18} < n < 2\times10^{20}$ cm^{-3}. At higher densities the FM phase is destabilized by the increasing role of the kinetic energy [76]. In particular, with the increasing electron density the difference between kinetic energies of the FM and PM phases increases. To illustrate this factor we note that in the simplest case of the total spin polarization twice more *k*-states are occupied in the FM phase (with 1 electron per *k*-vector) than in the PM phase (with 2 electrons per *k*-vector). Consequently, the corresponding Fermi wave vectors obey $k_F^{FM} = 2^{1/3} k_F^{PM}$, and the transition to the PM state lowers the kinetic energy by $2^{2/3}$ (see Fig. 3.12.). Therefore, the difference between the kinetic energies of FM and PM phases is $0.17\hbar^2 k_F^2 / m^*$, which obviously increases with the increasing electron density, i.e., with the decreasing lattice constant.

One can also consider a more realistic model of a band with a sinusoidal dispersion, which is a good approximation of the valence bands in of II-V compounds in the *zb*-phase (Fig. 3.10), *i.e.*, $E(k) = 2\varepsilon_0 \sin(kA)$, with $\varepsilon_0 = \varepsilon_F/2$. In this case,

$$\Delta\overline{E}^{FM-PM} = \frac{\varepsilon_0}{\pi^2 A n_{crit}}\left[k_F\left(2^{2/3}\sin(2^{1/3}k_F A) - \sin(k_F A)\right) + \frac{2k_F}{A}\left(2^{1/3}\cos(2^{1/3}k_F A) - \cos(k_F A)\right) - \right.$$
$$\left. - \frac{2}{A^2}\left(\sin(2^{1/3}k_F A) - \sin(k_F A)\right)\right]$$

where the first and the second term correspond to the Hartree-Fock energy of ferromagnetic and of paramagnetic situation, respectively. This expression allows one to find the critical concentration of free holes, n_{cr}, at which $\Delta\overline{E}^{FM-PM}$ vanishes. This occurs at the critical lattice constant a_{crit}, for which $A = \left(\frac{\pi}{24 n_{crit}}\right)^{1/3}$, and $k_F = \left(3\pi^2 n_{crit}\right)^{1/3}$. Significantly, the calculated values $\Delta\overline{E}^{FM-PM}$ using this simple model and the equilibrium lattice constants of *zb*-II-V crystals agree to within ~15% with the values ΔE^{FM-PM} from Table 3.1.

These arguments explain the disappearance of the magnetic moment at small lattice constants. Moreover, they may explain the lack of FM in *zb*-Be-V [3] and *zb*-Mg-V compounds, which have lattice constants smaller than the corresponding compounds of Ca, Sr, and Ba. Both *zb*-MgP and MgAs at equilibrium are paramagnetic because their lattice constants are smaller, and thus E_{kin} are larger, compared with these of CaP and CaAs, respectively, see Fig. 3.13.

In crystals, the destabilizing role played by E_{kin} is further enhanced by a second factor, which is the decrease of the effective mass m^* of free carriers with the decreasing lattice constant. This effect originates in the increase of the band widths due to stronger interatomic interactions. These arguments hold in II^A-V crystals with the zinc-blende structure, where the valence bands have sinusoidal-like shapes to a good approximation.

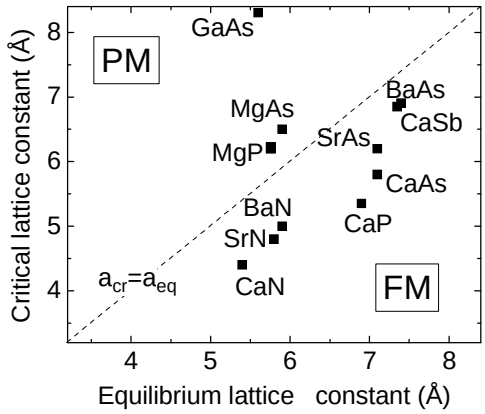

Fig. 3.13. Relation between the equilibrium a_{eq} and the critical a_{crit} lattice constants for zb –II^A-V compounds.

On the other hand, the energy bands in *rs*-II-V nitrides have a more complex topology. As an example we show in Fig. 3.14 both the band structure and the DOS for *rs*-CaN at the critical lattice constant a_{crit} for which the spin polarization vanishes. (The values of a_{crit} are given in Table II below). In this case there is an overlap of the conduction and valence states. In the spirit of the Stoner criterion, the relevant quantity is the DOS at the Fermi level. The comparison of the results from Figs. 3.12 and 3.14 illustrate well this point, since the DOS at the Fermi level decreases almost three times when the lattice constant decreases from a_{eq} = 5.0 to a_{crit} = 3.7 Å, driving the destabilization of the FM phase.

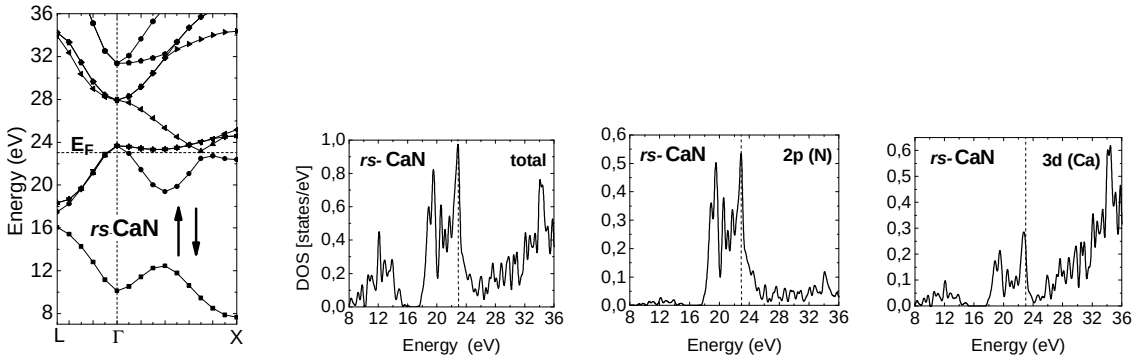

Fig. 3.14. Band structure of rs-CaN, and the total and partial densities of states at the critical lattice constant a_{crit} = 3.7 Å. Dashed lines indicate the Fermi energy.

The above discussion of role of the kinetic energy is general in character, and to a large degree independent of the crystal structure. In particular, it explains qualitatively the weaker stability of FM in the *rs*-II-V crystals, which follows from the smaller equilibrium atomic volumes found for this structure (and thus higher kinetic energies) as compared with the *zb* structure. In fact, the atomic volumes in the *rs* phase are smaller by about 15% compared to the *zb* phase.

In a broader perspective, the obtained results lead to a general question: why solids like Si or GaAs, made out of atoms that carry magnetic moments, are non-magnetic? In fact, the atoms constituting these crystals, Si, Ga, or As, have non-vanishing spin polarization according to the Hund's rule, and in a naïve picture one may expect that these crystals should be magnetic as well. Thus, we also analyze GaAs. The magnetic moment of GaAs is 4 μ_B per unit cell (when the spins of Ga and As are parallel in Fig. 3.15). In the region B, the magnetic moment drops from 4 to 2, and GaAs with 8 Å < a < 12 Å is ferromagnetic. The drop stems from the onset of hybridization of p(Ga) and p(As) orbitals; the band structure is 'reversed' in the sense that the Γ_1 band (which is the bottom of the conduction band at equilibrium) is below the Γ_{15} band (forming the top of the valence band at a_{eq}) and GaAs is metallic. For a < 8 Å, the level ordering is like this in Fig. 3.9, 8 electrons fill 4 valence bands, and GaAs is paramagnetic.

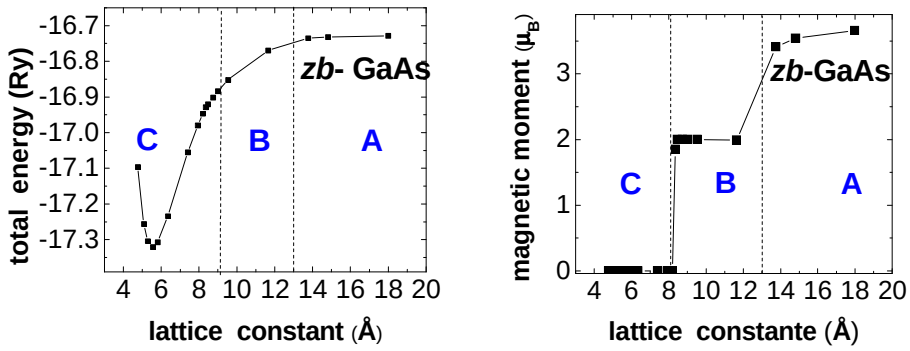

Fig. 3.15. Total energy and total magnetic moment per unit cell of zb-GaAs as function of the lattice constant.

3.2. Structural stability of II^A-V compounds

In contrast to III-V or II-VI compounds that typically crystallize in the *zb* structure, II-V compounds crystallize in variety of structures. Several II-V compounds assume the Zn_3P_2 phase, which is a primitive tetragonal lattice with 40 atoms in the unit cell, or a more complex Zn_3As_2, which is a body-center tetragonal structure with 160 atoms in the unit cell [7]. Materials with these structures are not magnetic. SrN has been observed in two phases, namely *rs* [10] and monoclinic [11, 12]. Magnetic II^{TM}-V compounds usually crystallize in the *NiAs* structure. This is the case of NiAs, CrAs, CrSb [8], and also of FM α-MnAs that crystallizes in the *NiAs* structure with alternating hexagonal planes of Mn and As atoms [9]. However, it is important to notice that with the help of epitaxial techniques of growth it is possible to synthesize these compounds in other structures that are metastable. For example, CrAs [85] and CrSb [86] layers have been fabricated in the metastable *zb* structure by molecular beam epitaxy in spite of the fact that the calculated total energy of this phase is at least 0.4 eV/atom higher than that of the ground state *NiAs* phase [87]. Turning to the case of II^{TM}-V nitrides we observe that the early transition metal mononitrides TiN and VN crystallize in the rock salt structure [88]. In particular, *rs*-ScN [89], *rs*-CeN [90], and *rs*-CrN [91] were grown by sputter deposition on MgO(001) substrates. Finally, the ground state phase of MnN is the rock salt structure with a weak tetragonal distortion [92, 93] and AFM ordering, reproduced by first principles calculations [94, 95]. The AFM ordering has also been found both for the *zb* [96] and for the wurtzite [97] metastable structures of MnN. Because of the variety of possible structures of II^A-V compounds, it is important to establish their low-energy phases. To this end we investigate here four structures, namely *zb*, *NiAs*, Zn_3P_2, and *rs*. We do not consider the wurtzite structure since its energy typically differs from that of *zb* by a few meV/atom only. Thu unit cells of the consider structure are shown in Fig. 3.16.

The calculated total energy as a function of the atomic volume for *zb*, *rs*, and the *NiAs* phases of CaN is presented in Fig. 3.17. We note that it is not possible to present E_{tot} of CaN in the Zn_3P_2 structure in this Figure because of the different stoichiometry of this phase. Figure 3.17 shows that the most stable phase is *rs*, while the *zb* phase is higher in energy by 0.75 eV/atom.

These results characterize other II^A-V compounds as well, see Table 3.2., and are similar to these obtained for ScN [103] and CaAs [3].

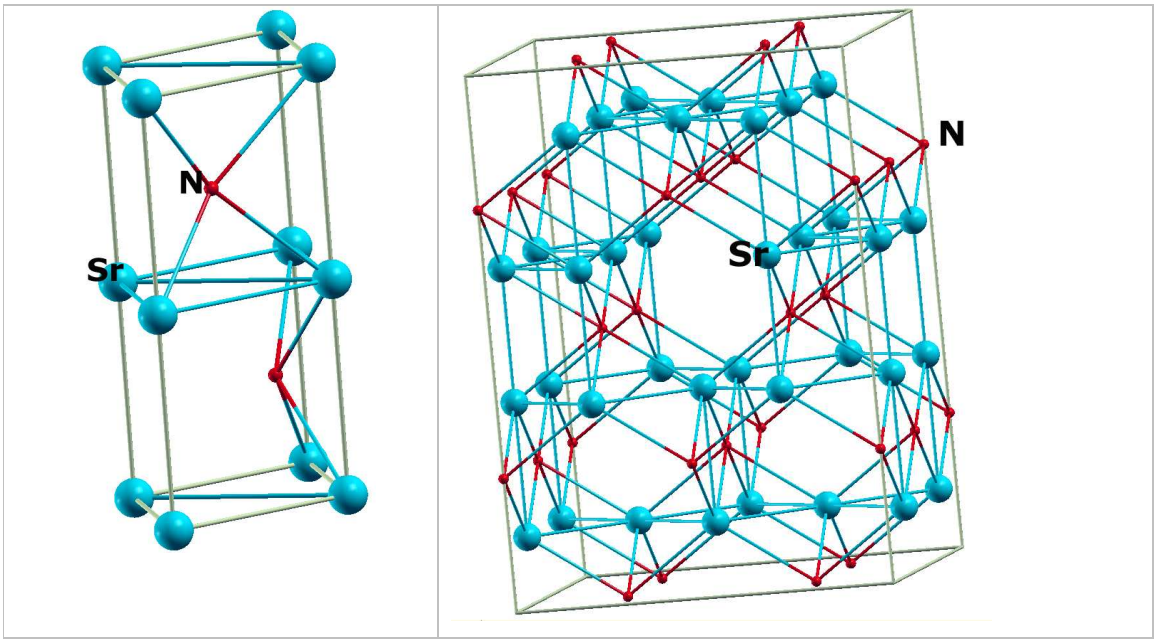

Fig. 3.16. These unit cells of NiAs and Zn_3P_2 structures.

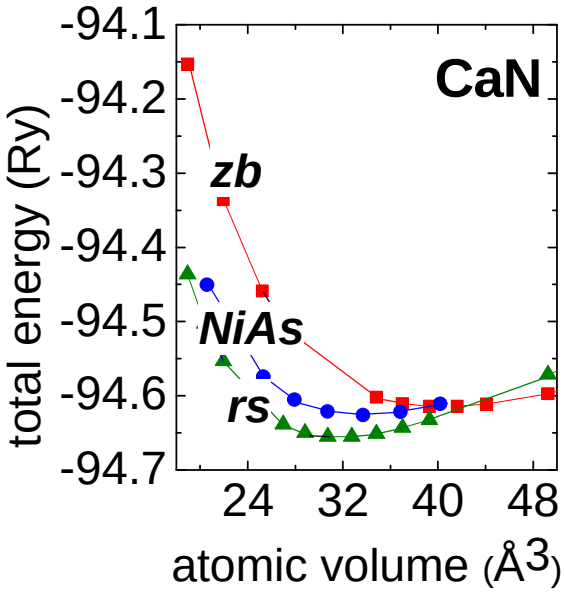

Fig. 3.17. Total energy (in Ry/2 atoms) as a function of the atomic volume for three structures of CaN.

The calculated lattice parameters are given in Table 3.2., along with cohesive energies per two atoms defined as

$$E_{coh}^{II-V} = 2\left(E_{tot}^{II-V} - n^{II}E_{at}^{II} - n^{V}E_{at}^{V}\right)/\left(n^{II}+n^{V}\right). \qquad (3.1)$$

Here E_{tot}^{II-V} is the total energy per unit cell of the considered compound, E_{at} is the energy of isolated atom, and n^{II} and n^{V} are number of atoms of groups II and V in the unit cell, respectively. Considering first the simple structures we find that for all compounds (except BaN) the *zb* phase is the less stable, *NiAs* is intermediate and *rs* is the most stable one.

Since we expect the magnetism to be the most stable for the II-V nitrides (see Section 3.1), I have also considered the computationally more demanding Zn_3P_2 phase for these compounds. For both BaN and CaN the Zn_3P_2 phase is more stable than the *rs*, with the difference in cohesive energies between the two phases of 0.032 and 0.075 eV/atom, respectively. In contrast, SrN in the *rs* phase is more stable by 0.055 eV/atom. The calculated cohesive energies of II-V nitrides are large compared to, *e.g.*, E_{coh}^{II-V} of Ca, which is -3.68 eV/2 atoms. This indicates that after being formed, the II-N crystals are expected to be stable due to the high energies of II-N bonds.

A second aspect of stability of a compound is displayed by its heat of formation ΔH_f^0, which indicates stability with respect to decomposition into bulk constituents. The heat of formation at T=0 K is obtained by considering the reaction to form (or decompose) a crystalline bulk II-nitride from (or into) its components, and is defined as

$$\Delta H_f^0 = E_{coh}^{II-V} - \left(n^{II}E_{coh}^{II} + n^{N}E_{bind}^{N_2}/2\right)/\left(n^{II}+n^{V}\right), \qquad (3.2)$$

where E_{coh}^{II-V} and E_{coh}^{II} are the cohesive energy per atom of the considered nitrides and of the group-II metal in its equilibrium structure, respectively, and $E_{bind}^{N_2}$ is the binding energy of the N_2 dimer. The obtained results for E_{coh}^{II} are -1.80, -1.62, and -1.85 eV/atom for Ca, Sr, and Ba in their equilibrium structures (fcc, fcc, and bcc, respectively). We also find that $E_{bind}^{N_2}$ is –4.9 eV/atom, in reasonable agreement with experimental data. Note that according to this definition a negative ΔH_f^0 implies that the compound is stable against decomposition into bulk constituents. The

calculated values of E_{coh}^{II-V} and ΔH_f^0 are given in Table 3.2. The results for BaN, SrN, and CaN show that the Zn_3P_2 structure is energetically more favorable than the *rs* phase, since its ΔH_f^0 is lower. From Table 3.2 it follows that the difference between ΔH_f^0 of the Zn_3P_2 and the *rs* structure is 0.77, 0.55, and 0.68 eV for CaN, SrN, and BaN, respectively. However, we stress that not only the Zn_3P_2 but also the *rs* phase is thermodynamically stable, which follows from the negative ΔH_f^0. Since the stoichiometries of these structures are different, the formation of one of them should critically depend on the conditions of growth. The *rs* structure is metastable, since the corresponding heats of formation are somewhat higher than those of the Zn_3P_2 phase. The energies of both the *zb* and the *NiAs* phases are about 0.3 eV/atom higher. Consequently, the relative stability of the *rs* phase of II^A-V nitrides justifies the analysis of their magnetic properties in Section 3.1. Finally, the calculated ΔH_f^0 are relatively low, similar to those of the recently synthesized PtN_2 crystals [104].

In Table 3.2 I also give the calculated equilibrium lattice parameters. For all crystals we find that the *NiAs* phase is strongly distorted, i.e., the *c/a* ratio is considerably larger than the ideal value 1.63. This distortion plays an important role in determining the magnetic properties: for the ideal value of *c/a* most of the systems are found to be FM, while the inclusion of the tetragonal distortion destroys the FM order, and the crystals are paramagnetic. Considering the Zn_3P_2 structure we find that the *c/a* ratio is very close to ideal value 1.41, but the internal atomic displacements inside the unit cell are large

Since II^A-V compounds in the *rs* phase are metallic (see Section 3.1) and have the high cubic symmetry, one may expect that the cooperative Jahn-Teller effect takes place and lowers the crystal energy. In order to check the stability with respect to the Jahn-Teller effect I have considered three types of distortions of the *rs* structure, namely (i) a typical tetragonal distortion in the [001] direction (which takes place, e.g., in MnN) [92, 93], (ii) a pseudo-cubic distortion in the (110) orientation after which the lattice parameters are $a = b = c = a_{eq}$ (*rs*-phase) and $\alpha \neq \beta$, $\gamma = 90°$, and (iii) a distortion of the nitrogen sublattice only, in which the N-N distances are reduced from the ideal value a_{eq}(*rs*-phase)/$\sqrt{2}$ (which is 3.8 Å in SrN) to 1.1 Å, which is the equilibrium bond length of the N_2 molecule. I investigated 8, 16, 32, 64- atoms supercells of

structure rock salt. I have taken into account this distortion because in several nitrides, such as SrN_2 [11,12] or HfN_2 [104], N atoms form nearest neighbor pairs. According to our results the ideal *rs* phase is stable with respect to all these symmetry-lowering distortions.

Table 3.2. Calculated equilibrium lattice parameters, critical lattice constant a_{crit} (in Å), cohesive energies, and heats of formation of II^A-V compounds. For hexagonal phases we give the values of both a_{eq} (in Å) and of *c/a* in two consecutive lines.

Phase	BaN	SrN	CaN	CaP	CaAs	CaSb
lattice parameters at equilibrium						
zb	5.92	5.82	5.40	6.88	7.14	7.41
NiAs	3.81	3.65	3.49	4.02	4.13	4.23
	1.73	1.93	1.83	2.13	2.13	2.23
Zn_3P_2	8.99	8.73	8.20			
	1.41	1.41	1.41			
rs	5.55	5.40	5.0	6.24	6.35	6.66
critical lattice constant						
zb	4.8	4.87	4.5	5.3	5.8	6.88
rs	5.18	4.34	3.7	5.9	6.35	7.4
cohesive energy (eV/2 atoms)						
zb	–6.85	–6.16	–6.74	–5.38	–5.12	–4.71
NiAs	–6.82	–6.17	–6.89	–5.92	–5.73	–5.41
Zn_3P_2	–7.19	–6.67	–7.63			
rs	–7.12	–6.78	–7.48	–6.20	–5.95	–5.53
heat of formation (eV/atom)						
Zn_3P_2	–1.05	–0.81	–1.55			
rs	–0.37	–0.26	–0.78			

Finally, I comment on the possibility of growing FM II^A-N nitrides. In most cases, the Zn_3P_2 phase is more stable than the *rs*. However, the different stoichiometries of the two phases imply that the formation of one of them, and in particular of the FM rock salt phase, should

strongly depend on the conditions of growth such as relative flux intensities. Moreover, in epitaxial growth the substrate and its structure play an important role and determine the structure of the epilayer. Consequently, the choice of appropriate epitaxial conditions should allow obtaining *rs*-II^A-V nitrides. More specifically, the lattice constants of *rs* CaN, SrN, and BaN (5.0, 5.4, and 5.55 Å.) are close to these of *zb*-InN (4.98 Å) [105], *zb*-GaP (5.45 Å), and *zb*-GaAs, (5.65 Å) respectively, which suggests their use as appropriate substrates. Also the a_{eq} of *rs*-CaP (6.24 Å) about only 4 % smaller than that of *zb*-InSb (6.47 Å). The possibility of synthesis of *rs*-II^A-V nitrides is supported by the growth of metastable phases by molecular beam epitaxy. This is the case of cubic MnTe or GaN, *zb*-CrAs [85] and *zb*-CrSb [86], to quote a few examples.

In this Part I have studied magnetic and electronic structures of a number of II^A-V compounds. Four crystal structures were considered: zinc-blende, *NiAs*, rock salt, and Zn_3P_2. In the *zb* structure, all the considered crystals are characterized by the total spin polarization of free holes. However, the energy of this structure higher than that of the *rs* phase, in which only II-V nitrides are spin-polarized. In order to understand the properties of the investigated crystals I have considered a very broad range of lattice constants, beginning from the case of almost separated atoms, and ending with this of highly compressed solids. A detailed analysis of the electronic structure and density of states revealed that the calculated spin polarization has the origin in the spin polarization of isolated group-V anions. At small lattice constants the magnetization vanishes because of two factors. First, the kinetic energy favors the non-polarized configuration of the electron gas, and the role of this effect increases with the increasing electron density. The second factor destabilizing magnetization at small lattice const.ants is the decreasing density of states at the Fermi level. Structural stability of the II^A-V compounds was analyzed by calculating both their cohesive energies and heats of formation. In most cases, the Zn_3P_2 phase is more stable than the *rs*, and in the Zn_3P_2 phase the spin polarization vanishes. However, the possibility of synthesis of *rs*-II^A-V nitrides is supported by the growth of metastable phases.

Part IV

Magnetism of monoclinic SrN

This part is devoted to molecular magnetism of SrN. In Part III, magnetic properties of the *zb*, *NiAs*, Zn_3P_2 and *rs* structures of SrN were studied. However, SrN and SrN_2 were recently synthesized, and their crystals structures are monoclinic and tetragonal for SrN and SrN_2, respectively [11, 12]. In this Part, magnetic properties of the experimentally determined structures are examined.

4.1. The crystal structure of SrN and SrN_2

The crystal structure of SrN is monoclinic (*m*) [11] that of SrN_2 is tetragonal (*t*) [11]. These structures are shown in Fig. 4.1. The monoclinic phase of SrN has 16 atoms per unit cell, 8 atoms of strontium and 8 atoms of nitrogen. The unit cell of tetragonal SrN_2 comprises 2 atoms of Sr and 4 atoms of N. In both structures the Sr ions form octahedra. In SrN_2, all N ions form dimers, which are a characteristic feature of dinitrides such as IrN_2 or PtN_2 [106,107]. In SrN, only half of N ions (denoted by N_{dim}) form dimers, while the remaining ions (denoted by N_{iso}) occupy centers of Sr octahedra with a coordination characteristic for the rock-salt phase. As a result of the different coordinations, the two types of N ions, N_{dim} and N_{iso}, are in different charge states, and SrN is a mixed valence compound.

In the calculations, Brillouin zone integrations were performed using a (2×6×4) *k*-point grid for *m*-SrN, and a (12×12×10) grid for *t*-SrN_2. I used the experimental lattice parameters a = 13.472 Å, b = 3.8121 Å, c = 6.7284 Å, and $\beta = 94.72^{\circ}$, [11] because as a rule GGA reproduces well the structural properties. Moreover, optimization of the parameters of this complex structure would require a substantial computational effort. To partially verify this assumption, the positions of all atoms in the unit cell were relaxed. Relaxation energy is 0.03 eV/atom and displacements of atoms from the experimental coordinates are minor. The largest displacements are found for Sr atoms, about 0.2 Å, and the bonds of the two N_2 dimers are longer by 6 % than the experimental

ones. The consistency between experiment and theory confirms both the identification of the structure and the expected accuracy of GGA. In the case of *t*-SrN_2, the calculations reproduce the experimental lattice parameters (a=3.8136 Å, c= 6.2855 Å) [11] to within 0.5 % and the energy of relaxation is very small (0.007 eV/atom).

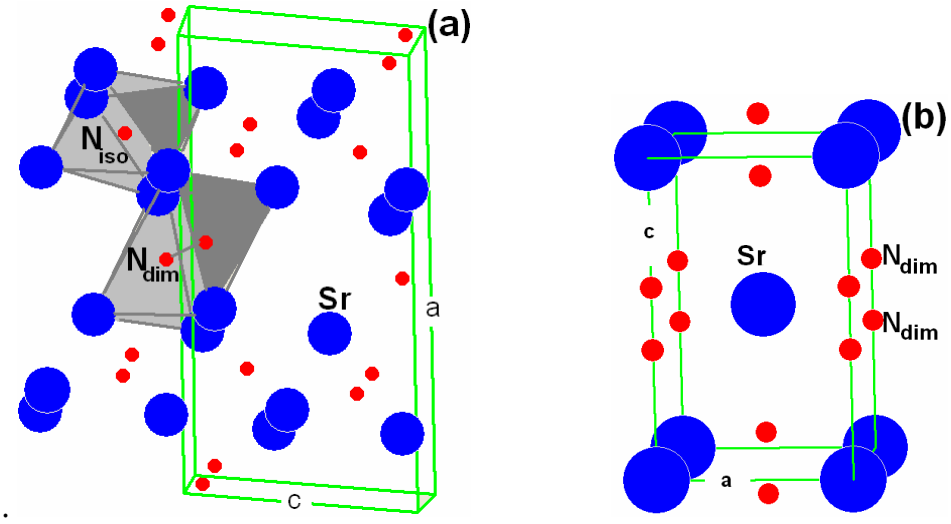

Fig. 4.1. Crystal structure of (a) m-SrN and (b) t-SrN_2. Big blue dots denote Sr and small red ones denote N. N ions forming dimers and isolated N ions are indicated by N_{dim} and N_{iso}, respectively.

Table 4.1. Calculated cohesive energies and heats of formation (eV/atom) of *m*-SrN and *t*-SrN_2.

	m-SrN	*t*-SrN_2
E_{coh}	-3.7	-4.3
ΔH_f^0	-0.88	-0.49

To analyze structural stability I calculated cohesive energy E_{coh} and heat formation ΔH_f^0 of *m*-SrN and *t*-SrN_2 using Eqs. 3.1 and 3.2. The results are given in Table 4.1. The negative values of ΔH_f^0 show that *m*-SrN and *t*-SrN_2 are stable with respect to decomposition. Moreover, ΔH_f^0 of *m*-SrN, -0.88 eV, is lower then that of the rock salt SrN, -0.26 eV. This agrees with experiment, and shows that rock salt phase is only metastable.

4.2. Magnetic properties of m-SrN

I first analyze electronic structure of *m*-SrN. The different coordinations of the two types of N ions in *m*-SrN, N_{dim} and N_{iso}, result in their different properties reflected in charge and spin densities. Contour plot of electron density, Fig. 4.2.a, shows the molecular bond of N_2, while the spherical shape of charge density around both N_{iso} and Sr indicates the ionic character of bonds between N_{iso} and its Sr neighbors.

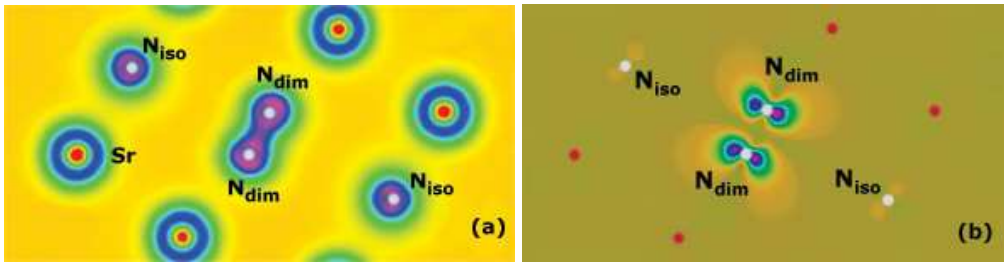

Fig. 4.2. Contour plot of (a) the charge density, and (b) the spin density of m-SrN unit cell in the y=0 plane. Sr and N atoms are presented by red and white dots, respectively. N-N dimer is in the middle of the unit cell.

This situation is confirmed by the total density of states (Fig. 4.3.a) and the density projected on individual atoms shown in Figs. 4.3.b-d. Hybridization between Sr and N orbitals is weak, and the lower valence bands are predominantly formed by one kind of atomic or molecular orbitals. Thus the ionic character of *m*-SrN the valence bands shown in Fig. 4.3 are relatively narrow, about 2.5 eV. The highest valence band is formed by 3 kinds of orbitals (*p* orbitals of isolated ions of nitrogen, *p* orbitals of dimmers N_2, and *d* orbitals of Sr). First, the states at about 1 eV below the Fermi energy E_F originate in $p(N_{iso})$ orbitals (Fig. 4.3.b) occupied with 6 electrons. This implies that N_{iso} are in the closed-shell 3- charge state, which follows from the symmetric of DOS's for up and down spins. The second contribution originates in 3*d* orbitals of Sr, and this contribution is not spin-polarized to a good approximation, see Fig. 4.3.d 3*d*(Sr) orbitals mainly form conduction bands. Fig. 4.3.c shows that the largest and spin-polarized contribution to DOS at the Fermi energy comes from the *p* states of N_2 dimers. Fig. 4.3.c shows a contribution to DOS of one ion of nitrogen that fours N_2 dimer, which amounts to about 0.6

states/eV. The unit cell contains 4 N ions. Total DOS at Fermi level is about 3 states/eV in agreement with the contribution from 2 dimers, 4* 0.6 ≈ 2.4 states/eV. Finally, the non-vanishing DOS at E_F indicates the metallic character of *m*-SrN.

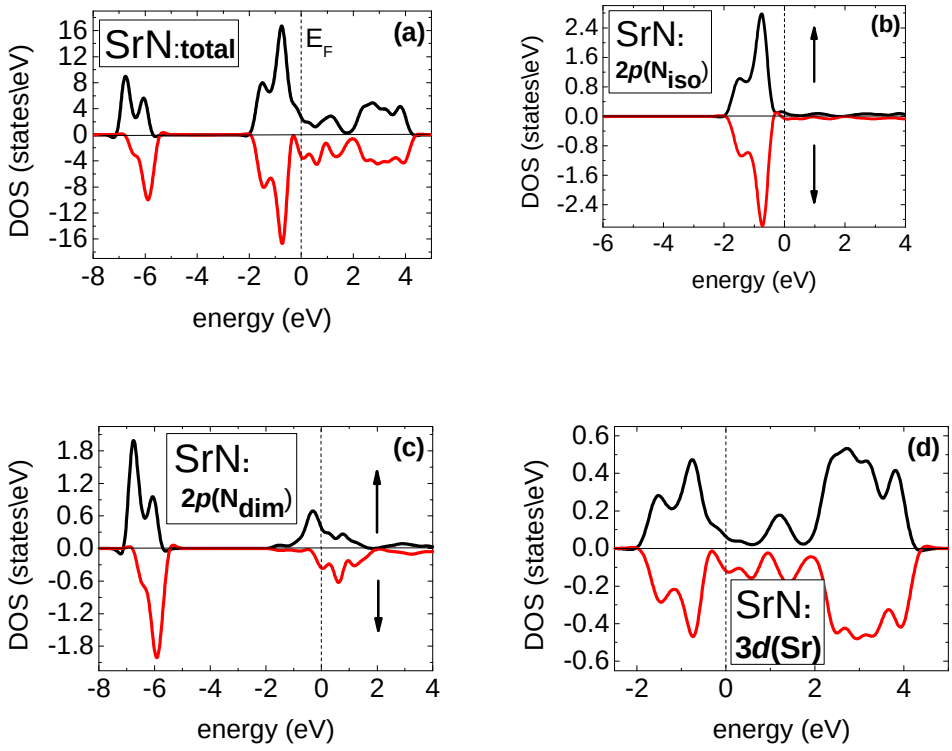

Fig. 4.3. Total density of states of FM m-SrN, and its projection on N_{iso}, N_{dim}, and Sr orbitals (a, b, c, and d, respectively). Arrows denote the spin-up and spin-down channels, and vertical dashed lines indicate the Fermi energy.

I now turn to magnetic properties of *m*-SrN. To find the ground state, several initial spin configurations were tried. In all cases, spin polarization of final configurations was non-vanishing, which demonstrates the presence of stable magnetic moments. These moments are strongly localized on N_2 dimers, Fig. 4.2.b, and may take on FM or AFM order. Those results shown in Fig. 4.3 hold for the FM phase, with different spin-up and spin-down DOS. Magnetic couplings between N_2 dimers were found using a unit cell doubled in the y-direction, *i.e.*, containing 32-atoms and shown in Fig. 4.4.a. This supercell allows studying both FM and 3 AFM configurations with various relative orientations of spins (Fig. 4.4.b). In *m*-SrN, each N_2

dimer has 2 first neighbors (1NNs) along the *y*-axis distant by *b*=3.8 Å. Next, it has 4 second neighbors (2NNs) in the (*x*,*y*) plane distant by 6.6 Å, and two 2NNs along the *c*-axis distant by *c*=6.7 Å. Thus, N_2 dimers form 1-dimensional and *y*-oriented 'chains' seen in Fig. 4.4.a. The six 2NNs are almost equidistant, and we assume that they are equivalent in terms of magnetic interactions. Using the Hamiltonian $H = \Sigma J_{ij} \mathbf{S}_i \cdot \mathbf{S}_j$, and assuming that the spin coupling is limited to the 1NNs and 2NNs, we find that the corresponding exchange constants, J_1 and J_2, are 16 and 1 meV, respectively.

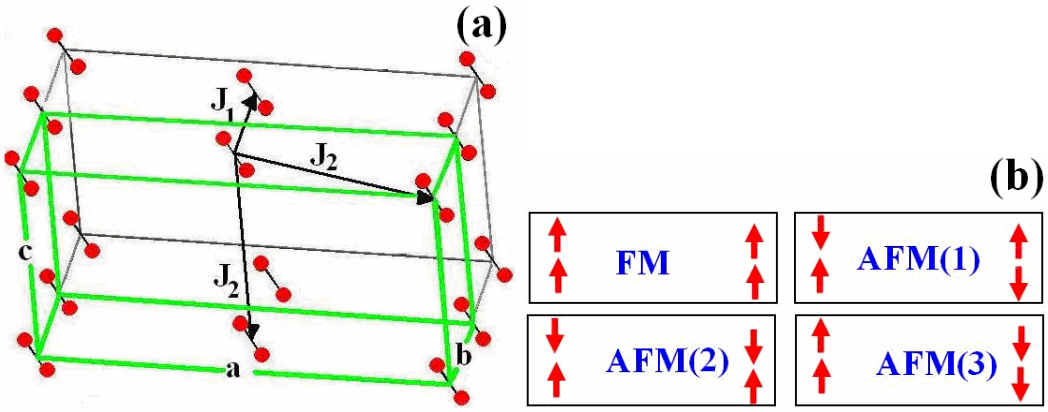

Fig. 4.4. (a) Sublattice of N_2 dimers in m-SrN. The unit cell is shown in green. J_1 and J_2 are the exchange constants, see text. (b)Top view along the c-axis FM and 3 AFM configurations with various relative orientations of spins in the N_2 sublattice. AFM (1) is the ground state.

The positive signs of *J* correspond to the AFM coupling. Thus, the coupling between N_2 within the *y*-oriented 'chains' is almost 20 times stronger than that with 2NNs. (This partially justifies our neglect of more distant dimers). To estimate the Neel temperature T_N we neglect the weak 'inter-chain' coupling, and use the mean-field approximation. This approach gives T_N=260 K for 1-dimensional 'chains'. The actual value may be somewhat different because typically the mean-field approximation overestimates T_N, [108] and the interaction with more distant neighbors is neglected. However, the estimated T_N is lower than room temperature, at which both *m*-SrN and *t*-SrN_2 are experimentally found to be paramagnetic [11].

According to the obtained results, the ground state phase is AFM, and the calculated magnetic moment of N_2 is 1.6 μ_B. The FM configuration is higher in energy by 82 meV/N_2,

and the N_2 dimers have a smaller the same magnetic moment, 1.2 μ_B. Finally, energy of the paramagnetic, *i.e.*, non-polarized, configuration is 117 meV/N_2 higher than that of AFM case.

Localization of the magnetic moments on N_2 dimers may suggest that the magnetic order is determined by the dipole-dipole coupling, which is not included in the DFT calculations. The contribution of the dipole-dipole coupling was calculated for FM and AFM(1) phases using the corresponding theoretical magnetic moments of N_2, 1.6 μ_B for AFM and 1.2 μ_B for FM. Thus, the magnetic moment of N_2 is higher in AFM than in FM. Since Hamiltonian $H \sim S^2$ (S is the total spin), then it explains that the phase with highest magnetic moment will be more stable [97]. Results show that the energy of AFM is lower by 18 meV/N_2 than that of FM. This is about 4 times smaller than 82 meV/N_2 obtained from the calculations, which indicates that the dominant magnetic coupling is mediated by delocalized states from the vicinity of the Fermi level, and that dipole-dipole interaction provides only an additional contribution stabilizing the AFM order.

4.3. Origin of magnetism of m-SrN

Electronic and magnetic structures of *m*-SrN can be interpreted based on energies of orbitals of an isolated N_2 molecule that are shown in Fig. 4.5. In a neutral N_2 molecule, the σ and π bonding combinations of *p*(N) orbitals are occupied. These orbitals give rise to the valence bands, with two resolved peaks, at about −6 eV below E_F, which are shown in Fig. 4.3.a. In the 2− charge state, the lowest antibonding orbital, π^*, is occupied with 2 electrons, and σ^* is about 1 eV higher in energy. The most important feature of this configuration is the stabilization of the high-spin state of the two electrons by the strong exchange coupling. Consequently, the magnetic moment of N_2^{2-} is 2 μ_B, with the same electronic configuration and magnetic moment as those of a neutral O_2 molecule. In *m*-SrN, the π^* and σ^* molecular states of N_2 are broadened by hybridization with neighbors, and the spin-up and spin-down states overlap, see Fig. 4.3.d. The Fermi energy falls within the overlap region. This implies that there is a transfer of electrons from spin-up to spin-down states, which reduces the spin

moment per N_2 from 2 to 1.6 μ_B in the AFM and 1.2 μ_B in the FM phase. Finally, the magnetic moments of N_{iso} ions vanish because of their closed-shell configuration in the 3– charge state.

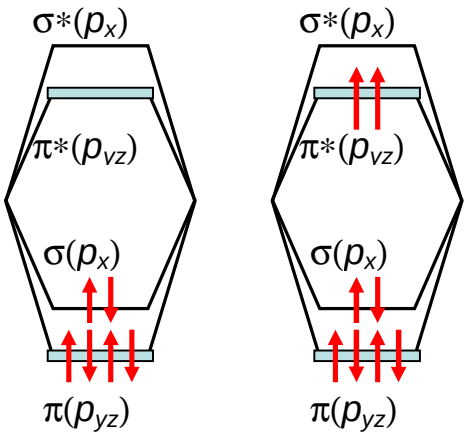

Fig. 4.5. Scheme of the electronic structure of an N_2 molecule in the neutral and in the $\tilde{2}$ charge state.

4.4. Magnetic properties of t-SrN_2

Density of states of the second investigated nitride, SrN_2, is shown in Figs. 4.6.a and 4.6.b. Energy bands derived from orbitals of N_2 dimers are similar to those in SrN. Stochiometry of SrN_2 implies that N_2 dimers are in the 2- charge state, as in SrN, and therefore one could expect that magnetic moments of the dimers are similar in both compounds. However, the calculated spin polarization of SrN_2 vanishes. This is attributed to the fact that the atomic volume of SrN_2 is smaller that that of SrN. More precisely, the distances between a N ion and its Sr neighbors are 2.61 and 2.94 Å in SrN, while in SrN_2 they are 2.53 and 2.76 Å, where the shorter distance corresponds to the N-Sr bond along the dimer axis. Shorter bonds imply a higher degree of hybridization of quasi-molecular N_2 orbitals and broader bands. Both factors counter-act the spin polarization of N_2 dimers. In fact, the π*-derived peak in the upper valence band, well-resolved in SrN, is smeared out in SrN_2, see Figs. 4.3.c and 4.6.b. This in turn implies a higher overlap between spin-up and spin-down states. In other words, in SrN_2 hybridization dominates the exchange splitting. This conclusion is confirmed by the fact that an increase of the lattice constant by 8 % from equilibrium induces a non-vanishing spin polarization in SrN_2.

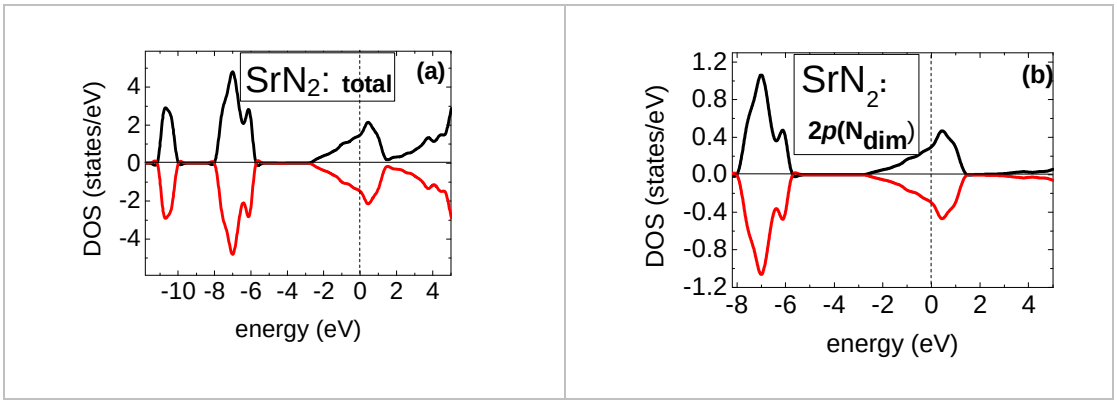

Fig. 4.6. (a) Total density of states of SrN_2. (b) Its projection on p (N_{dim}) are shown in and. Arrows denote the spin-up and spin-down channels and vertical dashed lines indicate the Fermi energy.

The results obtained here and in Part III allow pointing out conditions that favor non-vanishing spin polarization in a bulk crystal without magnetic ions. First, the crystal should contain species with partially filled open-shell orbitals. These orbitals may be of quasi-atomic character, which is the case of *rs*-SrN, or quasi-molecular ones in Rb_2O_6 [14] or in *m*-SrN. Second, only light atoms from the second row of the periodic table (i.e., C, N, O, and F) should lead to magnetization. This is because the compactness of their valence *p* shells induces high energies of spin polarization. The third critical factor is the atomic volume (or the lengths of bonds between N and its neighbors), which should be large enough to prevent a high hybridization of spin-polarized orbitals with surrounding. In the opposite case, the broadening of bands is larger than the exchange splitting, and the spin polarization vanishes. This is the case of SrN_2.

Summarizing, GGA calculations of the magnetic structure of the recently synthesized *m*-SrN indicate that this compound is a molecular antiferromagnet. Magnetic moments are localized on N_2 dimers. This stems from the occupation of the $\pi^*(N_2)$ antibonding orbitals with 2 electrons in the high-spin configuration, which is not destroyed by hybridization with Sr neighbors. On the other hand, *t*-SrN_2 is paramagnetic since stronger hybridization dominates spin polarization effects.

Part V

High-spin configuration of cation vacancies

Here I theoretically investigate the prospects of high-spin configuration of cation vacancies in *zb*-GaAs, GaP, GaN, AlN, and BN, and *w*-GaN, AlN, BN, ZnO, and BeO.

Formation of a cation vacancy, V_{cation}, results in formation of 4 dangling bonds of the 4 anion neighbors of the vacancy, Fig. 5.1. They combine into a non-degenerate level a_1 and a triply degenerate level t_2, which is higher in energy. Energies of a_1 and t_2 relative to the top of the valence band (TVB) depend on the type of vacancy, and on the crystal. Typically, for V_{cation} in most III-V and II-VI semiconductors, a_1 is fully occupied and is a resonance with the valence band, and t_2 is in the band gap and is occupied by three or four electrons for neutral V_{cation} in III-V or II-VI compounds, respectively. Moreover, as it was pointed out in Part I, in some cases electrons assume high-spin configurations, *i.e.*, their spins are arranged parallel in accord with the Hund's rule.

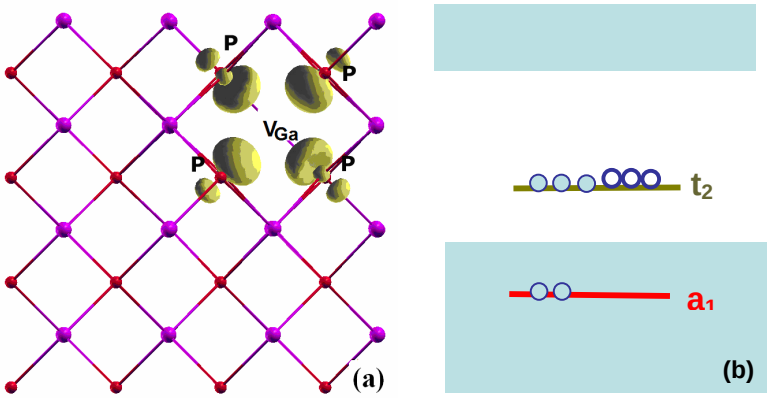

Fig. 5.1. Typical electronic structure of a cation vacancy in zb-III-V semiconductors. Four sp^3 orbitals of four neighbor's anions (a) introduce four energy levels, a singlet a_1 and a triplet t_2 (b). Filled and empty circles in (b) indicate occupied and empty states, respectively.

In the case of a spin-polarized vacancy, t_2 splits into spin-up ($t_{2\uparrow}$) and spin-down ($t_{2\downarrow}$) states by the exchange coupling by $\Delta\varepsilon_{ex} = t_{2\downarrow}\text{-}t_{2\uparrow}$. In this case, also a_1 splits into spin-up ($a_{2\uparrow}$) and

spin-down ($a_{2\downarrow}$) states. In the case when $t_{2\uparrow}$ is a resonance state, $\Delta\varepsilon_{ex}$ is defined as $2*(t_{2\downarrow}-t_2)$ because the energy $t_{2\uparrow}$ is not possible to be exactly defined.

To study the stability of various spin configurations of vacancies we calculate the spin polarization energies ΔE^{FM-PM}. ΔE^{FM-PM} is defined as the difference between the total energies of the vacancy in the high-spin and spin-non-polarized configuration. The high-spin state is stable if $\Delta E^{FM-PM} < 0$ and $\Delta\varepsilon_{ex} \neq 0$. The calculated electronic and magnetic properties of the vacancies are given in Tables 5.1-5.7, and in Figures 5.2-5.4, 5.7-5.10.

5.1. Electronic structure and spin states of neutral vacancies

In this Section I analyze the electronic structure of neutral cation vacancies. Charged vacancies are discussed in Section 5.2.

5.1.1. Neutral V_{cation} in zinc-blende III-V semiconductors

I start by summarizing the electronic structure of neutral cation vacancies in *zb*-III-V semiconductors. The calculated electronic structures of V_{cation} are shown in Fig. 5.2. Additionally, the calculated parameters are given in Table 5.1.

(i) **V_{Ga} in GaAs**. Vacancy-induced singlet a_1 is a resonance with the valence band. The energy of t_2 is 0.4 eV above the top of the valence band. In GaAs, the high-spin state is unstable, $\Delta\varepsilon_{ex}$ is zero, and the triplet state is occupied by 2 electrons with parallel spins and one electron with opposite spin. In this case, the initially imposed high-spin configuration decays into the low-spin state. Thus, V_{Ga} in GaAs has a low-spin configuration with the total spin S=½.

(ii) **V_{Ga} in GaP**. Here t_2 is 0.3 eV above TVB. However, in this case the high-spin state is stable, with ΔE^{FM-PM}= -0.06 eV, and t_2 is split into spin-up and spin-down states by the exchange $\Delta\varepsilon_{ex}$ equal to 0.19 eV. So, $t_{2\downarrow}$ is empty and $t_{2\uparrow}$ is occupied by 3 electrons, and V_{Ga} in GaP has a high-spin configuration with total magnetic moment μ_{tot} is 3 μ_B, see Table 5.1. This fact agrees with the known experimental data [62].

Table 5.1. Electronic and magnetic characteristics of V_{cation} in *zb*-III-V semiconductors ($\Delta E^{FM\text{-}PM}$, $\Delta\varepsilon_{ex}$, t_2, and Δ_{TVB} in eV; μ_{tot} and μ_{abs} in μ_B).

	GaAs (216 at)	GaP (216 at)	GaN (512 at)	AlN (512 at)	BN (512 at)
$\Delta E^{FM\text{-}PM}$	0	-0.06	-0.69	-0.93	-0.82
$\Delta\varepsilon_{ex}$	0	0.19	0.78	1.3	0.92
t_2	0.41	0.31	0.22	0.54	0.52
μ_{tot}	0	3.0	3.0	3.0	3.0
μ_{abs}	0	3.21	3.47	3.3	3.36
Δ_{TVB}		0.16	-0.01	-0.01	-0.07

(iii) $\boldsymbol{V_{Ga}}$ **in GaN** introduces t_2 in the band gap at 0.22 eV above the TVB. The high-spin state is stable with $\Delta E^{FM\text{-}PM}$= -0.69 eV. The exchange-induced spin splitting of t_2 into $t_{2\uparrow}$ and $t_{2\downarrow}$ is large, about 0.78 eV. Consequently, and in contrast to GaP, the energy of $t_{2\uparrow}$ is a resonance degenerate with the valence band and $t_{2\uparrow}$ is occupied with 3 electrons, while $t_{2\downarrow}$ is 0.6 eV above the TVB and is empty. Thus, V_{Ga} in GaN has a high-spin configuration with the total spin 3/2.

(iv) $\boldsymbol{V_{Al}}$ **in AlN**. t_2 is 0.54 eV above TVB. The high-spin state is stable with the $\Delta E^{FM\text{-}PM}$= -0.93 eV, which is larger than in GaN. Also $\Delta\varepsilon_{ex}$, 1.3 eV, is larger than in GaN. $t_{2\uparrow}$ is a resonance occupied by 3 electrons with parallel spins, and V_{Al} in AlN is in a high-spin state with the total spin 3/2. Next, in AlN the a_1 singlet is in the valence band for non-polarized calculation but close to the TVB, inclusion of spin polarization causes that a_1 is spin-split as well, and $a_{1\downarrow}$ is in the band gap at 0.25 eV above TVB (see Fig. 5.2). $a_{1\downarrow}$-$t_{2\downarrow}$ splitting is 0.95 eV.

(v) In the case of $\boldsymbol{V_B}$ **in BN**, t_2 is 0.52 eV above TVB, $\Delta\varepsilon_{ex}$ = 0.92 eV, and $\Delta E^{FM\text{-}PM}$= -0.82 eV, thus, similar to the V_{Ga} and V_{Al}, V_B has a stable high-spin state with S=3/2. In this case, $t_{2\uparrow}$ is very close to the top of the valence band.

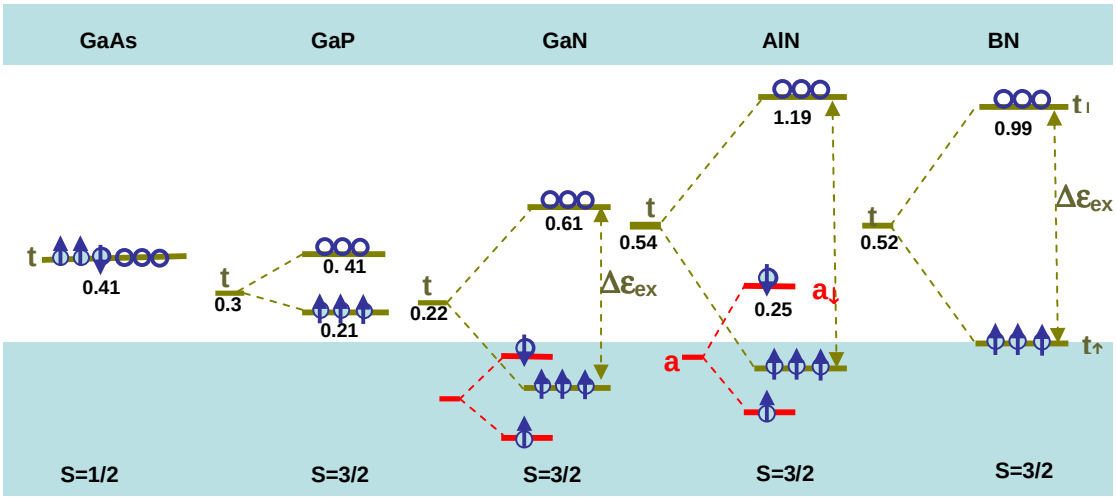

Fig. 5.2. Electronic structures of neutral V_{cation} in zb-III-V semiconductors. t and a denote the t_2 and a_1 states, respectively. The numbers give the calculated energies relatively on TVB, in eV. Conduction band is shown only schematically, and does not reflect the actual value of the band gap. Spins of electrons are indicated by arrows, empty spheres indicate unoccupied states.

Summarizing, in all considered cases V_{cation} introduces t_2 in the band gap at about 0.3 eV above TVB. In GaAs, both the spin polarization and the exchange-induced spin splitting $\Delta\varepsilon_{ex}$ vanish. In contrast, the high-spin state is stable for V_{Ga} in GaP, with $\Delta E^{FM\text{-}PM}$= -0.06 eV and $\Delta\varepsilon_{ex}$ = 0.19 eV. Stability of the high-spin state is much more pronounced in the nitrides, since $\Delta E^{FM\text{-}PM}$ is one order of magnitude higher and $\Delta\varepsilon_{ex}$ is about 4 times larger than in GaP.

5.1.2. Neutral V_{cation} in wurtzite III-V semiconductors

I now turn to cation vacancies in III-N nitrides in the wurtzite structure. In general, the results for *zb* and *w* structures are similar in terms of spin polarization energies and position of vacancy levels, as expected. Differences are partially due to the smaller size of the supercell used for the wurtzite structure. Due to hexagonal symmetry of wurtzite, the triplet t_2 is split into a doublet *e* and a singlet *a* with a splitting energy of 0.15, 0.05, and 0.3 eV for vacancies in GaN, AlN, and BN, respectively.

Table 5.2. Electronic and magnetic characteristics of V_{cation} in *w*-III-V semiconductors.

	GaN (128 at)	AlN (128 at)	BN (128 at)
ΔE^{FM-PM}	-0.63	-0.85	-0.54
$\Delta\varepsilon_{ex}$	1.14	1.4	0.94
e	0.28	0.45	0.45
μ_{tot}	3.0	3.0	3.0
μ_{abs}	3.38	3.27	3.31
Δ_{TVB}	-0.02	-0.01	-0.2

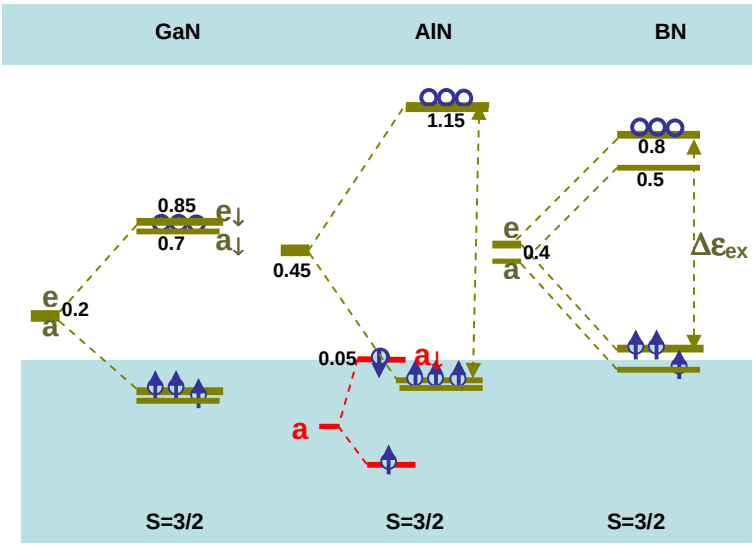

Fig. 5.3. Electronic structure of neutral V_{cation} in w-III-N nitrides. Conduction band is shown only schematically, and does not reflect the actual value of the band gaps. Spins of electrons are indicated by arrows, empty spheres indicate unoccupied states.

The calculated electronic structures are shown in Fig. 5.3, where a singlet and a doublet (bold lines) states show by green lines *e*, is 0.28, 0.45, and 0.45 eV for V_{Ga}, V_{Al}, and V_B, respectively (see Table 5.2). The high-spin states are stable for vacancies in *w*-nitrides because ΔE^{FM-PM} are negative, and are -0.65, -0.85, and -0.55 eV for V_{Ga}, V_{Al}, and V_B, respectively, and corresponding exchange-induced spin splittings $\Delta\varepsilon_{ex}$ are 1.15, 1.4, and 0.95 eV. Consequently, in all cases, the $t_2\uparrow$-derived $e\uparrow$ and $a\uparrow$ levels are resonances and have 3 electrons with parallel spins, and vacancies in *w*-III-N nitrides have high-spin configuration with the total spin S=3/2. Next, similar to *zb*-AlN, V_{Al} in *w*-AlN introduces $a_1\downarrow$ very close to TVB. The $a_1\downarrow$-$e_2\downarrow$ splitting is 1.1 eV.

5.1.3. Neutral V_{Zn} in w-ZnO and V_{Be} in w-BeO

I also considered cation vacancies in wurtzite ZnO and BeO. In these cases, the states of the vacancy are built from the oxygen *p* orbitals and are occupied by 6 electrons. The vacancy introduces a singlet a_1 inside the valence band and triplet t_2 in the band gap close to TVB. The triplet t_2 is split by the wurtzite crystal field into a doublet and a singlet states with a small splitting energy of ~0.1 eV. The calculated energy levels are shown in Fig. 5.4. In the spin-nonpolarized case, t_2 is 0.22 and 0.36 eV above TVB in ZnO and BeO, respectively. In both crystals, the triplet is spin-split by the exchange interaction, however $t_{2\uparrow}$ are not resonances, because $\Delta\varepsilon_{ex}$ are smaller than for III-V nitrides, and amount to 0.11 and 0.44 eV for V_{Zn} and V_{Be}, respectively. ΔE^{FM-PM} = -0.04 eV in ZnO and -0.2 eV in BeO. Thus, in both crystals the vacancies have stable high-spin states with S=1 and total magnetic moment is 2 μ_B (see Table 5.3) because $t_{2\uparrow}$ is occupied by 3 electrons, and $t_{2\downarrow}$ by 1 electron.

The calculated higher stability of the spin polarization in BeO can be ascribed to its smaller lattice constant (a=2.7 Å, c= 4.38 Å) than that of ZnO (a=3.25 Å, c=5.2 Å), which should lead to a stronger electron-electron coupling.

Table 5.3. Electronic and magnetic characteristics of V_{Zn} in *w*-ZnO and V_{Be} in *w*-BeO.

	ZnO (128 at)	BeO (128 at)
ΔE^{FM-PM}	-0.04	-0.2
$\Delta\varepsilon_{ex}$	0.11	0.44
t_2	0.22	0.36
μ_{tot}	2.0	2.0
μ_{abs}	2.1	2.17
Δ_{TVB}	-0.11	-0.1

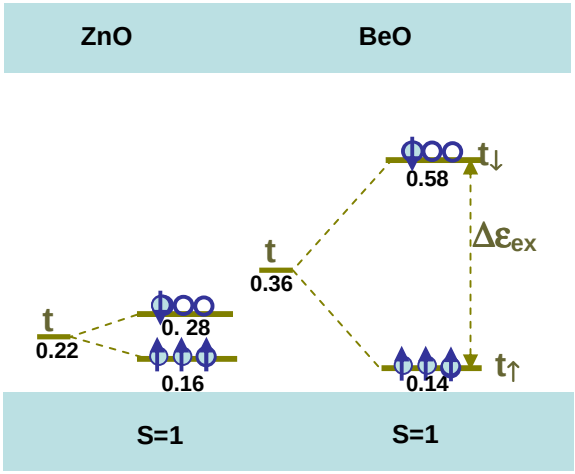

Fig. 5.4. Energy level diagram V_{Zn} in w-ZnO, and V_{Be} in w-BeO. The small hexagonal splittings are not shown. Conduction band is shown only schematically, and does not reflect the actual value of the band gap. Spins of electrons are indicated by arrows, empty spheres indicate unoccupied states.

Finally, for the take of completeness, we also analyzed V_{Si} in *zb*-SiC. In this case we used only a 64-atom supercell. It was shown that V_{Si} has stable high-spin state with S=1. Our results agreement with these of Refs. [67, 68], where a detailed analysis of V_{Si} in *zb*-SiC is given.

5.1.4. Spin density of cation vacancies

Figures 5.5 and 5.6 display the spin density of vacancies in the considered crystals. One can see that the main contribution is given by the orbitals of the neighbors of the vacancy. This contribution is strongly localized in the case of V_{Ga} in GaP and V_{Si} in SiC. In contrast, in the III-V nitrides the vacancy-induced triplet state $t_{2\uparrow}$ is a resonance in the valence band. In this case, in agreement with the resonant character of the vacancy-induced levels, the spin polarization is not strongly localized on sp^3 orbitals of the vacancy neighbors, but is fairly long-ranged. This feature is highlighted in Fig. 5.5.c. The electrons from the $t_{2\uparrow}$ level are hybridized with the states from the upper part of the valence band, which are mainly formed from the *p*(N) orbitals. Spin polarization of not only the nearest neighbors of the vacancy but also of the more distant N ions is clearly visible in Fig. 5.5.c. However, the dominant contribution of the localized part of the wave function explains why the spin polarization persists even in the case when t_2 is a resonance. A situation similar to that in GaN takes place in both ZnO and BeO, where the t_2 level is very close in energy to the TVB and has the same symmetry. The resulting hybridization is reflected in the fairly delocalized character of the spin density in Fig. 5.6.c.

Moreover, we calculated total magnetic moment of system (μ_{tot} is the sum of projections an axis of spin magnetic moments) and absolute magnetic moment of system (μ_{abs} is the sum of absolute values of spin magnetic moments). In all cases the total magnetic moment is not equal to the absolute magnetic moment, see Tables 5.1-5.7. For example, V_{cation} in *zb*-III-N nitrides have μ_{tot} =3 μ_B, but μ_{abs} is about 3.4 μ_B. The difference between μ_{abs} and μ_{tot} is small, about 10 %, but it shows that the spin polarization has an oscillatory behavior, and is due to the spin polarization of the states from the top of the valence band induced by the magnetic moment of the vacancy.

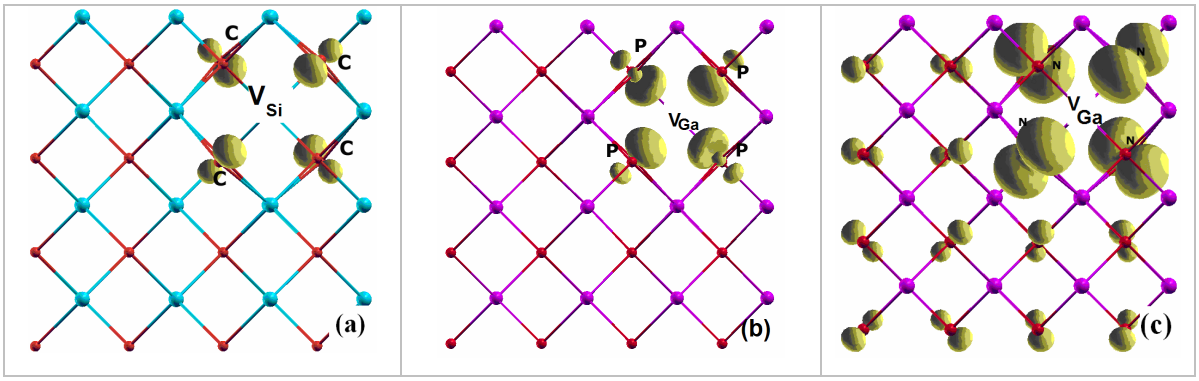

Fig. 5.5. Spin density of (a) V_{Si} in zb-SiC, (b) V_{Ga} in zb-GaP and (c) V_{Ga} in zb-GaN.

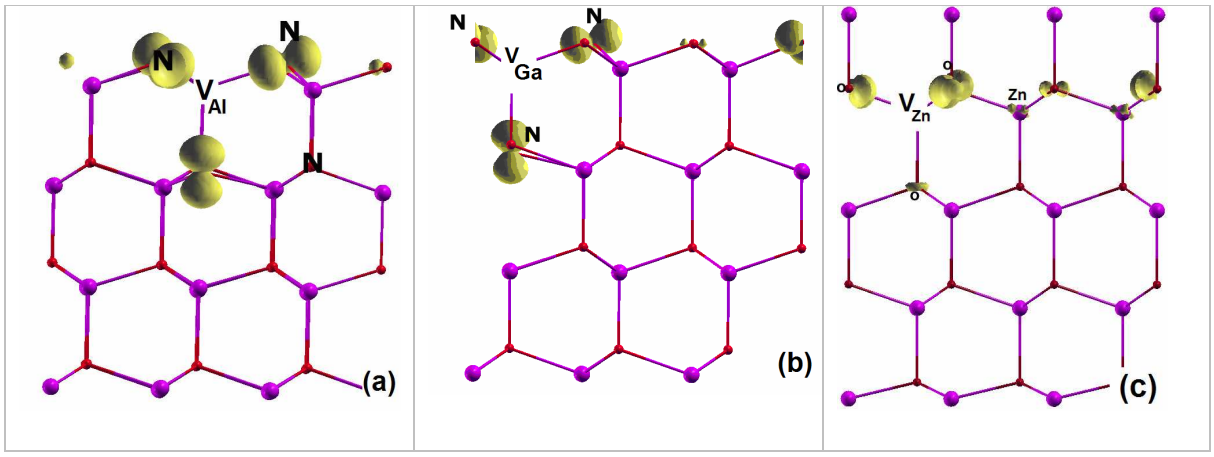

Fig. 5.6. Spin density of cation vacancy in (a) w- AlN, (b) w- GaN, and (c) w-ZnO.

Finally, the spin polarization reflects the symmetry of the crystal: in the *zb* structure the spin polarization of vacancy has an isotropic character (Fig. 5.5.c), but in the wurtzite structure it is anisotropic, and only the “in plane” spin polarization takes place, see Fig. 5.6.

Due to the long-range tail of the spin polarization, there is a possibility of magnetic coupling between vacancies, which may lead to their magnetic order. But this possibility is an open question and may occur only for high concentrations of vacancies [60].

5.2. Spin states of charged vacancies

Here I turn to the dependence of the spin polarization and electronic structure of vacancies on the charge state.

(i) **Charged V_{Ga} in GaP**. Fig. 5.7 illustrates the results for three occupations of the triplet states of V_{Ga} in GaP that range from q=1+ to q=1-. As discussed previously, the exchange coupling induces a high-spin state for a neutral vacancy with the total spin 3/2. In contrast, for the positively and negatively charged vacancies we find that $\Delta E^{FM\text{-}PM}$ =0, and the exchange splitting of triplet states vanish (see Table 5.4). Thus, in those cases the vacancies have the low-spin configurations with the vanishing total spins, and indeed the high-spin configurations other than 3/2 have not been observed.

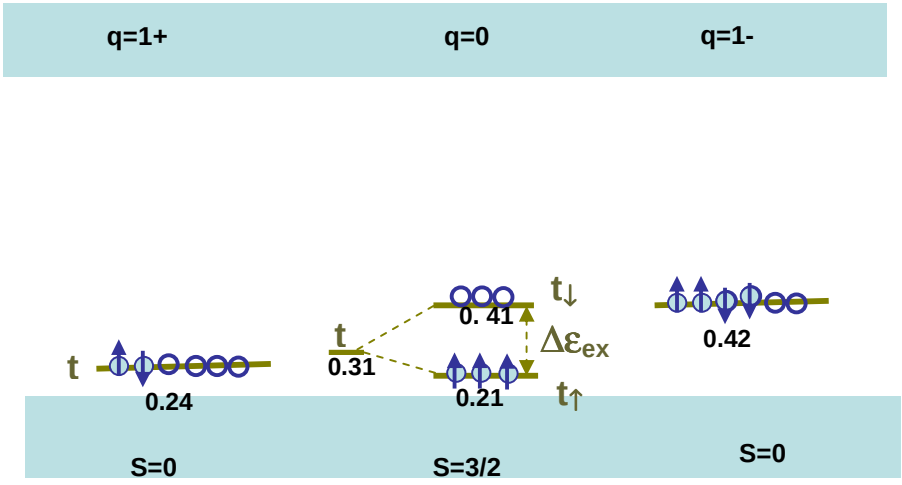

Fig. 5.7. Energy level diagram of charged V_{Ga} in GaP. Conduction band is shown only schematically, and does not reflect the actual value of the band gap. Spins of electrons are indicated by arrows, empty spheres indicate unoccupied states.

Table 5.4. Electronic and magnetic properties of charged V_{Ga} in *zb*-GaP.

q	1+	0	1-
ΔE^{FM-PM}	0.008	-0.06	0.007
$\Delta\varepsilon_{ex}$	0	0.19	0
t_2	0.24	0.31	0.42
μ_{tot}	0	3.00	0
μ_{abs}	0	3.21	0
Δ_{TVB}		0.16	

(ii) **Charged V_{Ga} in GaN.** In GaP or SiC, cation vacancies can assume the q=+1 charge state in *p*-type samples because the $t_{2\uparrow}$ triplet is in the band gap. On the other hand, in GaN, AlN, and BN the $t_{2\uparrow}$ state is a resonance in the valence band, and formation of a positively charged vacancy is not possible, since $t_{2\uparrow}$ is always occupied with 3 electrons. However, I have also analyzed the case when one additional hole per vacancy is added to the system in order to check the impact of *p*-type doping on the magnetic properties of vacancies. In the following, this situation is referred to as "q=+1" charge state. In particular, the additional hole may be coupled with the spin of the vacancy, and this coupling may be or ferromagnetic or antiferromagnetic.

The electronic structure of V_{Ga} in *zb*-GaN strongly depends on its charge state, see Fig. 5.8. The energy of triplet state t_2 increases by 1 eV, from 0.13 eV to 1.12 eV, when the charge state changes from q="1+" to 2-, which is due to the increasing intracenter electron-electron repulsion. In contrast to V_{Ga} in GaP, the exchange coupling induces high-spin state not only for a neutral vacancy, but also for all charged states. (Of course, for q=3- the t_2 state is fully occupied, and spin polarization vanishes). The exchange-induced spin splitting of t_2 into $t_{2\uparrow}$ and $t_{2\downarrow}$ is 0.98, 0.78, 0.78, and 0.47 eV for q=1+, 0, 1-, and 2- respectively, see Table 5.5. As it is shown in Fig. 5.8, due to the increase of the Coulomb repulsion, $t_{2\uparrow}$ is not a resonance for V^{1-}_{Ga} and V^{2-}_{Ga}. In those cases, the wave function of t_2 is expected to be more localized than for q=0, and the calculated exchange splitting is smaller than for the q=0 state.

Next, also the energy of the vacancy-induce singlet a_1 rises with the increasing charge state: a_1 is a resonance for q=1+ and 0. For q=1-, $a_{1\downarrow}$ is above the top of the valence band, while for q=2- both $a_{1\uparrow}$ and $a_{1\downarrow}$ are in the gap. One may also notice that in the latter case the spin polarization of the singlet, about 0.4 eV, is close to that of the triplet.

Considering the q=2- case, it should be stressed that in spite of the fact that the total spin is 1/2, the electronic configuration corresponds to the *high-spin state*. This follows from the non-vanishing exchange splitting of t_2 by $\Delta\varepsilon_{ex}$ = 0.47 eV, see Fig. 5.8. This situation is analogous to that of a Ni atom with 9 electrons on the 3*d* shell.

Finally, for "q=+1" the $a_{1\downarrow}$ state is very close to the TVB, and the accuracy of the calculations is too small to provide the exact spin state, since the calculated magnetic moment is 2 or 4 μ_B (see Table 5.5) depending on the details of calculation.

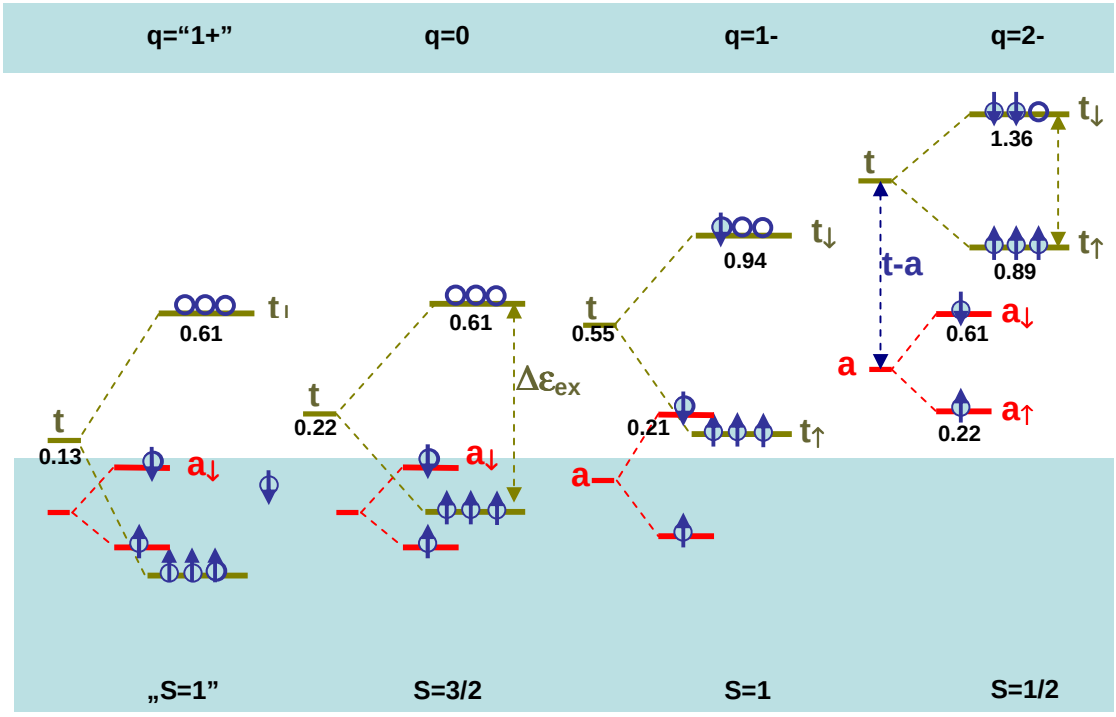

Fig. 5.8. Energy level diagram of charged V_{Ga} in GaN. The conduction band is shown only schematically, and does not reflect the actual value of the band gap.

Table 5.5. Magnetic properties of charged V_{Ga} in *zb*-GaN.

	″1+″	0	1-	2-
ΔE^{FM-PM}	-0.65	-0.69	-0.39	
$\Delta\varepsilon_{ex}$	0.98	0.78	0.78	0.47
t_2	0.13	0.22	0.55	1.12
μ_{tot}	″2.0″/″4.0″	3.0	2.0	1.0
μ_{abs}	″4.26″	3.44	2.31	1.17
Δ_{TVB}	-0.01	-0.01	0.04	0.03

(iii) **Charged V_{Al} in AlN.** The electronic structure of charged V_{Al} shown in Fig. 5.9 is very similarly to that of V_{Ga} in GaN. For all charge states the high-spin state is stable since ΔE^{FM-PM} are negative, see Table 5.6, but the absolute values are somewhat higher than in GaN, which is indicative of the higher stability of spin polarization. The energy of the vacancy-induced a_1 singlet is higher than in GaN. Interestingly, for all charge states cases $a_{1\downarrow}$ is in the band gap, and the $t_{2\downarrow}$-$a_{1\downarrow}$ splitting is about 0.95 eV.

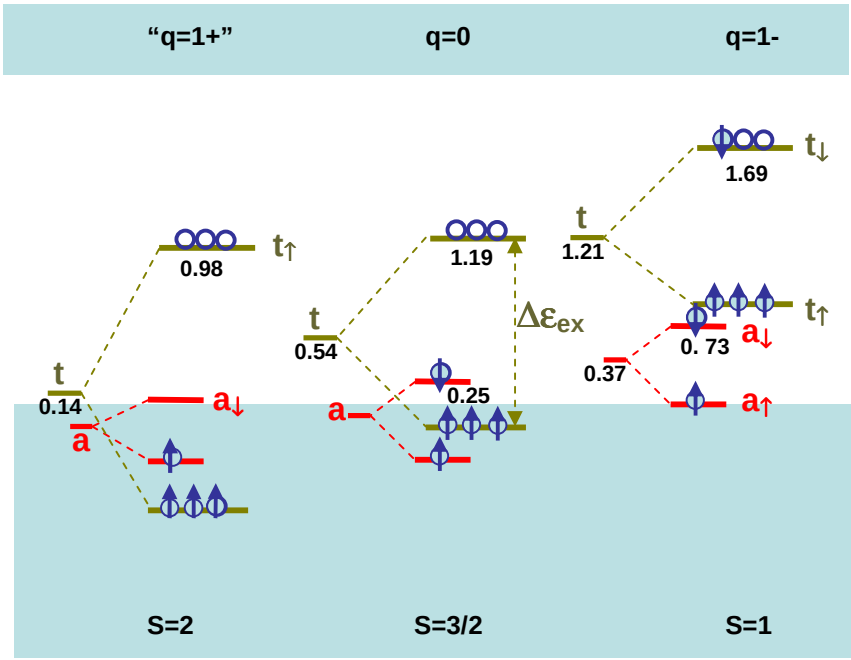

Fig. 5.9. Energy level diagram of charged V_{Al} in AlN. The conduction band is show only schematically, and does not reflect the actual value of the band gap.

Table 5.6. Magnetic properties of charged V_{Al} in *zb*-AlN.

q	"1+"	0	1-
ΔE^{FM-PM}	-0.7	-0.93	-0.45
$\Delta\varepsilon_{ex}$	1.68	1.3	0.96
t_2	0.14	0.54	1.21
μ_{tot}	4.0	3.0	2.0
μ_{abs}	4.4	3.3	2.21
Δ_{TVB}	0.0	-0.01	0.05

(iv) **Charged V_B in BN.** Electronic structure of charged V_B is shown in Fig. 5.10, and it is similar to that of the cation vacancy in GaN and AlN. ΔE^{FM-PM} is negative in all cases (see Table 5.7), and the high-spin states are stable. Moreover, for all charge states a_1 is inside the valence band, which demonstrates that the t_2-a_1 splitting is larger than 1.4 eV.

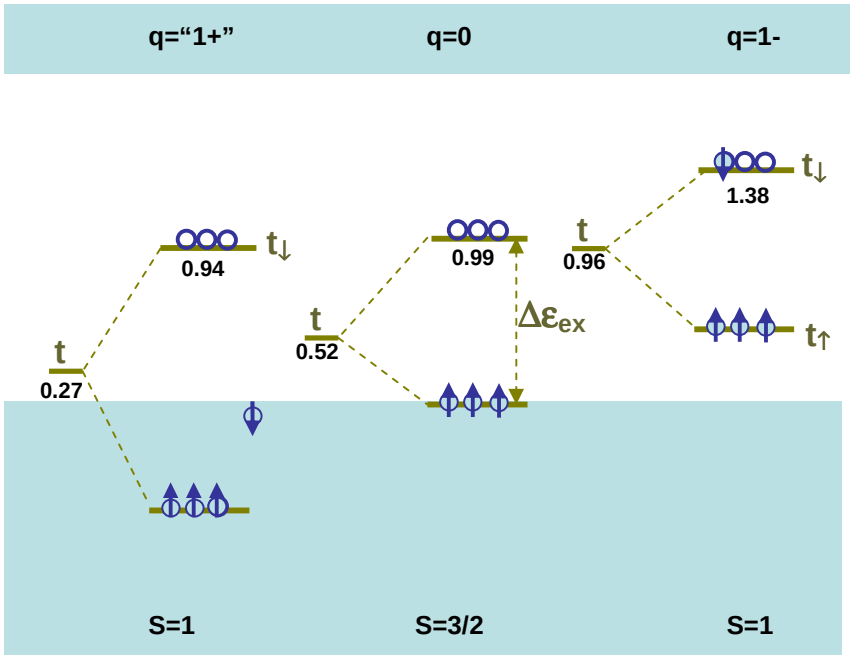

Fig. 5.10. Energy level diagram of charged V_B in BN. Conduction band is show only schematically, and does not reflect the actual value of the band gap.

Table 5.7. Magnetic properties of charged V_B in *zb*-BN.

	"1+"	0	1-
ΔE^{FM-PM}	-0.51	-0.82	-0.39
$\Delta\varepsilon_{ex}$	1.34	0.94	0.84
t_2	0.27	0.52	0.96
μ_{tot}	2.05	3.0	2.0
μ_{abs}	3.49	3.36	2.23

5.3. The exchange splitting of TVB

The obtained results show that the TVB splits into spin up $\varepsilon_{TVB}\uparrow$ and spin down $\varepsilon_{TVB}\downarrow$ levels by the energy Δ_{TVB}, which is given in Tables 5.1-5.7. The effect results from the coupling between the vacancy-induced t_2 level and the states from the top of the valence band. This coupling, or 'quantum repulsion', is possible because both states have the same symmetry, and is illustrated in Fig. 5.11. The absolute values of the splitting Δ_{TVB} are in general small, *i.e.*, they do not exceed 0.1 eV, and Δ_{TVB} is the highest in GaP and BN. The sign of Δ_{TVB} stems from the relative energies of t_2 and the TVB. When $t_{2\uparrow}$ is in the gap, the highest state of valence electrons is the spin-down state, *i.e.*, spin of a free hole is parallel to that of t_2 and the vacancy-hole coupling in ferromagnetic. An opposite situation holds when $t_{2\uparrow}$ is a resonance, since in this case the sign of the splitting of the TVB changes, see Fig. 5.11. In other words, the sign of the *p-p* exchange interaction between the vacancy and the free holes changes. This effect is analogous to that of the *p-d* exchange coupling between Mn ion and holes, which has the opposite sign in GaAs:Mn and in GaN:Mn.

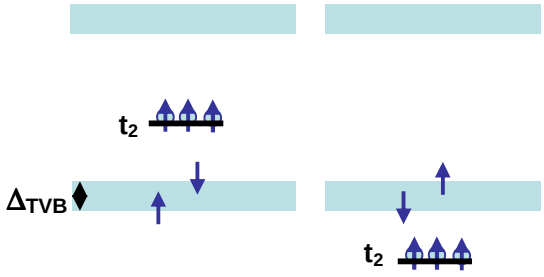

Fig. 5.11. The dependence of sign of the splitting of the TVB on the energy of the triplet state.

5.4. The energy of spin polarization of vacancy vs exchange splitting

Figure 5.12 summarizes the calculated values of $\Delta E^{FM\text{-}PM}$ and $\Delta\varepsilon_{ex}$ for all the considered cases. The figure shows that $\Delta E^{FM\text{-}PM}$ correlates with the exchange splitting $\Delta\varepsilon_{ex}$, since $\Delta E^{FM\text{-}PM}$ increases with the increasing $\Delta\varepsilon_{ex}$. This correlation takes place because the energy gain $\Delta E^{FM\text{-}PM}$ induced by the formation of the high-spin state is partially provided by the energy gain of the electronic contribution to the total energy. This mechanism is illustrated in Fig. 5.12.

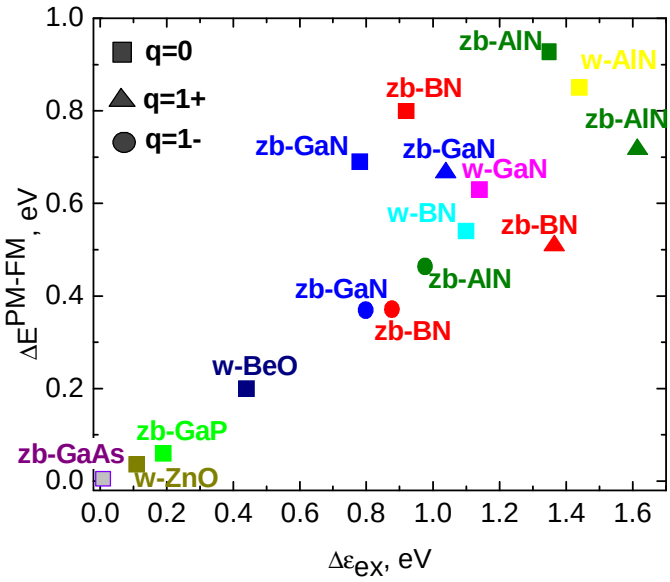

Fig. 5.12. The dependence of the energy of spin polarization of vacancies on exchange splitting of t_2 levels for various charge states.

In particular, Fig. 5.13 explains why the calculated energy gains $\Delta E^{FM\text{-}PM}$ are the highest when the t_2 state is occupied with 3 electrons, while for other occupations the high-spin state is less stable, or it vanishes like in GaP. This argument also accounts for the lower energy of spin polarization of a neutral vacancy in ZnO and BeO (where t_2 is occupied with 4 electrons) than that of a neutral vacancy in III-V nitrides (where t_2 is occupied with 3 electrons).

If this mechanism would account for entire energy of spin polarization, the relation $\Delta E^{FM\text{-}PM} = (3/2)\Delta\varepsilon_{ex}$ should be obeyed for neutral V_{cation} in III-V systems. However, from my results it follows that this mechanism accounts for about one half of $\Delta E^{FM\text{-}PM}$ (for both neutral and charged states), which indicates that other factors play an important role.

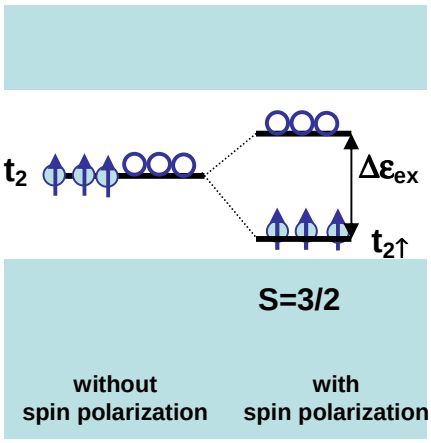

Fig. 5.13. The scheme explaining the energy gain from the electronic contribution of triplet state to the spin polarization of the vacancy.

5.5. Details of calculation. The effect of relaxation of structure

To verify the convergence of the results with respect to the size of the supercell, the calculations were performed for cells with 64, 216, and 512 atoms for *zb* structure, and 72 and 128 for the wurtzite structure. The results for *zb* are given in Table 5.8. The calculations showed that in the case of GaP convergent results are obtained for the supercell with 64 atoms because of the localized character of the t_2 state. In the remaining cases, the t_2 level is a fairly delocalized resonance, and thus only the results obtained with 512-atom supercells are expected to be converged due to the interaction of vacancy-induced states from the neighboring supercells. For technical reasons, in the case of the wurtzite structure I was not able to use supercells larger than 128 atoms.

Table 5.8. Electronic and magnetic characteristics of V_{cation} in *zb*-III-V semiconductors ($\Delta E^{FM\text{-}PM}$, $\Delta\varepsilon_{ex}$, t_2 in eV; μ_{tot} and μ_{abs} in μ_B).

	GaAs	GaP	GaN	AlN	BN
512 atom supercell (*zb*)					
$\Delta E^{FM\text{-}PM}$			-0.69	-0.93	-0.82
$\Delta\varepsilon_{ex}$			0.78	1.3	0.92
t_2			0.22	0.54	0.52
μ_{tot}			3.0	3.0	3.0
μ_{abs}			3.47	3.3	3.36
216 atom supercell (*zb*)					
$\Delta E^{FM\text{-}PM}$	0	-0.06	-0.85		
$\Delta\varepsilon_{ex}$	0	0.19	0.94		
t_2	0.41	0.31	0.22		
μ_{tot}	0	3.0	3.0		
μ_{abs}	0	3.21	3.47		
64 atom supercell (*zb*)					
$\Delta E^{FM\text{-}PM}$	0	-0.06	-0.21		
$\Delta\varepsilon_{ex}$	0	0.062	0.86		
μ_{tot}	0	0.60	3.0		
μ_{abs}	0	0.62	3.3		

Effects of atomic relaxation

I also analyzed the effect of relaxation of the vacancy neighbors on the value of $\Delta E^{FM\text{-}PM}$ and on the distance between the vacancy and its first and second neighbors. The results of calculations of $\Delta E^{FM\text{-}PM}$ and the energy of relaxation ΔE_{relax} for *zb*-III-N nitrides are given in Table 5.9. ΔE_{relax}, *i.e.*, the difference between total energies of the system without and with relaxation, was calculated for low- and high-spin configurations. One can see that without relaxation $\Delta E^{FM\text{-}PM}$ is -0.81, -0.94, and -0.99 eV for V_{Ga}, V_{Al}, and V_B, respectively, *i.e.*, it increases with the decreasing distance between N ions because of the increasing electron-electron coupling. In the case of GaN and BN, the relaxation decreases $\Delta E^{FM\text{-}PM}$ by 15 and 19 % for V_{Ga} and V_B, respectively, which stems from the fact that the outward displacement of N ions decreases the overlap between the broken bonds, and consequently reduces the exchange interaction. On the other hand, the effect of relaxation on $\Delta E^{FM\text{-}PM}$ is very small in AlN in spite of

the fact that the displacement of N neighbors is close to those in GaN and BN. Analysis of the electronic structure shows that in this case before the relaxation the $a_{1\downarrow}$ singlet in a resonance, but after the relaxation it rises in energy and is located in the band gap at 0.25 eV above the TVB. This in turn leads to a stronger localization of the wave function of a_1, and consequently enhances the exchange interactions within the vacancy orbitals. The two factors, *i.e.*, the decrease of ΔE^{FM-PM} caused by the outward displacement of N ions, and its increase caused by the localization of the a_1 state, almost cancel.

Table 5.9. The effect of the relaxation on ΔE_{relax} and ΔE^{FM-PM} (eV). 512-atom supercell.

	ΔE_{relax}		ΔE^{FM-PM}	
	PM	FM	*without relaxation*	*with relaxation*
V_{Ga}	0.61	0.45	-0.81	-0.69
V_{Al}	0.78	0.77	-0.94	-0.93
V_B	1.0	0.82	-0.99	-0.8

After the relaxation, the distance between the vacancy and the first (*l*), second (*m*), and third (*k*) neighbors of a neutral vacancy change. Those distances are show in Fig. 5.14. The first and third neighbors are nitrogen atoms. The second neighbors are cation atoms. The results of calculation are given in Table 5.10. In all cases, the relaxations are fully symmetric, and it mainly consists in the pronounced outward relaxation of first neighbors by 10.1, 12, and 9.6 % for V_{Ga}, V_{Al}, and V_B, respectively. The distances to the second and third neighbors change by about -0.5 and 0.2 %, respectively, for V_{Ga}; 0.3 and 0.46 %, V_{Al}; -0.8 and 0 %, V_B.

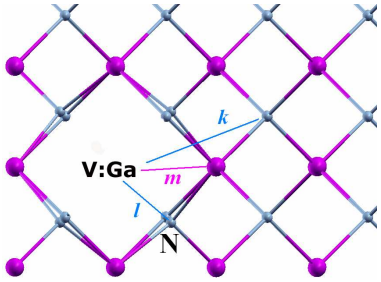

Fig. 5. 14. The gallium vacancy after relaxation.

Table 5.10. The effect of the relaxation on the distance between the vacancy and the first, second, and third neighbors of vacancy (Å).

	l		m		k	
	before relax	after relax	before relax	after relax	before relax	after relax
V_{Ga}	1.97	2.17	3.21	3.20	3.77	3.77
V_{Al}	1.90	2.13	3.10	3.11	3.63	3.65
V_B	1.57	1.71	2.56	2.54	3.00	3.00

In this Part I have analyzed the origin and the stability of high-spin states of cation vacancies. The calculations explain the experimental data for V_{Ga} in GaP and V_{Si} in SiC, and predict the high-spin state for vacancies in III-N nitrides and II-O oxides. The vacancy-induced states may be located either in the band gap or within the valence band forming resonant states. The energy of t_2 influences the degree of localization of the spin density, and to some extend the stability of high-spin states. From the calculated values of $\Delta E^{FM\text{-}PM}$ for *zb*-GaAs, GaP, and GaN it follows that $\Delta E^{FM\text{-}PM}$ decreases with the increasing of atomic number of anion, since it vanishes in GaAs and it is highest in GaN, -0.69 eV. This trend corresponds to the trend exhibited by the energy of the spin polarization of isolated As, P, and N atoms, which was discussed in Part III. Thus, the high-spin states of vacancies, which may be regarded as local spin polarization, and the global spin polarization of II-V crystals analyzed in the first part of my Thesis, shear a common physical origin, which is the strong exchange interaction of compact *p* electrons of light anions.

Part VI

Summary

This Thesis is devoted to the problem of magnetism in systems that do not contain transition metal atoms. In fact, magnetism based on *s* and *p* electrons only was experimentally observed and/or theoretically predicted to exist in a number of solids. My main goal was to confirm earlier theoretical results, to understand the mechanism responsible for the non-vanishing spin polarization in several crystals, and to provide predictions regarding potential materials that may exhibit this effect. To answer these problems, the calculations have been performed within the framework of density functional theory, using both the local spin density and the generalized gradient approximations for the exchange and correlation effects.

A detailed analysis of magnetic and electronic structure of a large number of II^{A}-V compounds in several crystallographic phases was performed. The results indicate that most of the considered crystals in the zinc blende phase are characterized by the total spin polarization of free holes. However, there is a critical question regarding the thermodynamic (*i.e.*, structural) stability of these open-shell structures relative to the closed-shell insulating and non-magnetic ones. Structural stability of the II^{A}-V compounds was analyzed by calculating their cohesive energies and heats of formation. For all antimonides, arsenides, and phosphides, the Zn_3P_2 phase is considerably more stable than the *rs*, and in the Zn_3P_2 phase the spin polarization vanishes. However, properties of II^{A}-V nitrides are different, the rock-salt structure is only weakly metastable, and possibly may be obtained by using epitaxial techniques. This suggestion is supported by a successful epitaxial growth of a variety of metastable phases of solids.

In order to understand magnetic properties of the investigated crystals I have considered a very broad range of lattice constants, beginning from the case of isolated atoms, and ending with this of highly compressed solids. From the obtained results it follows that the non-vanishing spin polarization has the origin in the spin polarization of isolated group-V anions. Atomic spin polarization, known as the Hund's energy, is the strongest for compact *p*-orbitals of light atoms from the second row of the Periodic Table, which explained why only compounds that contain C,

N, and O are expected to be spin-polarized. At small lattice constants the magnetization vanishes because of two factors. First, the kinetic energy favors the non-polarized configuration of the electron gas, and the role of this effect increases with the increasing electron density. The second factor destabilizing magnetization at small lattice constants is the decreasing density of states at the Fermi level, as predicted by the Stoner criterion.

Moreover, the recently synthesized SrN crystallized in the monoclinic structure, and contains both isolated N ions and N_2 dimers. An analysis of the magnetic properties of the *m*-SrN indicates that this compound is a molecular antiferromagnet. Magnetic moments are localized on N_2 dimers. This stems from the occupation of the $\pi^*(N_2)$ antibonding orbitals with 2 electrons in the high-spin configuration, which is not destroyed by hybridization with Sr neighbors.

The second part of the Thesis is devoted to the *local* spin polarization, namely to the high-spin states of vacancies. Typically, defects in semiconductors assume low-spin configurations, with the total spin 0 or 1/2. High-spin states with S=3/2 of cation vacancies were observed in several semiconductors two decades ago, but the effect was not explained. Based on the results obtained for bulk II-V crystals one can expect that the effect is also due to the strong spin polarization of light anions. To confirm this prediction, formation and stability of high-spin states of cation vacancies were investigated for BN, AlN, GaN, GaP, ZnO, BeO.

Formation of a cation vacancy results in formation of dangling bonds of the anion neighbors of the vacancy, which typically combine into a singlet state in the valence band and triplet state t_2 in the band gap close to the top of the valence band. The energy of triplet state depends on an anion of matrix and it decreases with the increased electronegativity of anion. The performed calculations show that high-spin state is stable in the case of a neutral V_{Ga} in GaP and a negatively charged V_{Si} in SiC, in agreement with experiment, but not in GaAs, again in agreement with experiment. Moreover, the calculations also predict that high-spin states are stable for V_{cation} in III-N nitrides and II-O oxides, due to the strong spin polarization of light anions pointed out above. More specifically, the analysis shows that spin density of vacancy is localized on sp^3 orbitals of neighbor's anions. In crystals, in which both the vacancy-induced $t_{2\uparrow}$ and $t_{2\downarrow}$ states are in the band gap (GaP or SiC), their wave functions are strongly localized on

those orbitals. When $t_{2\uparrow}$ is resonance state degenerate with the valence band, which is the case of the nitrides, the wave functions have both the localized part and the extended tails. Moreover, the spin polarization reflects the symmetry of the crystal: in the zinc blende structure the spin polarization of vacancy has an isotropic character, but in the wurtzite structure it is anisotropic, and only the “in plane” spin polarization takes place. Finally, the dependence of the spin state on charged state of vacancy was investigated. It was found that the high-spin state of V_{Ga} in GaP is stable only for the neutral vacancy. In contrast, in the nitrides, due to the much stronger spin polarization of N than that of P in GaP, the vacancy high-spin states are stable for charge states ranging from q=1+ to 2-.

The obtained results demonstrate that the physical origin of both effects, the spin polarization of bulk II^A-N nitrides and high-spin state of vacancy in III-N nitrides and II-O oxides, is the same, and consists in the strong spin polarization of *p* orbitals of light atoms from the second row of the periodic table (B, C, N, O).

Bibliography

[1] K. Kukasabe, M. Geshi, H. Tsukamoto, and N. Suzuki, J. Phys. C: Condens. Matter **16**, 5639 (2004).

[2] Volnianska, P. Jakubas, and P. Bogusławski, J. Alloys Compd. **423**, 191 (2006).

[3] M. Sieberer, J. Redinger, S. Khmelevskyi, and P. Mohn, Phys. Rev. B **73**, 024404 (2006).

[4] O. Volnianska and P. Bogusławski, Phys. Rev. B **75**, 224418 (2007).

[5] M. Geshi, K. Kusakabe, H. Nagara, and N. Suzuki, Phys. Rev. B. 76, 054433, (2007).

[6] G. Y. Gao, K. L. Yao, E. Şasioglu, L. M. Sandratskii, Z. L. Liu, and J. L. Jiang, Phys. Rev. B **75**, 174442 (2007).

[7] K. Sieranski, J. Szatkowski, and J. Misiewicz, Phys. Rev. B **50**, 7331 (1994).

[8] B.-G. Liu, Phys. Rev. B **67**, 172411 (2003).

[9] A. K. Das, C. Pampuch, A. Ney, T. Hesjedal, L. Daweritz, R. Koch, and K. H. Ploog, Phys. Rev. Lett. **91**, 087203 (2003).

[10] J. Gaude, P. L'Haridon, Y. Laurent, J. Lang, Rev. Chimie Minerale **8**, 287 (1971).

[11] G. Auffermann, Yu. Prots, and R. Kniep, Angew. Chem. Int. Ed. **40**, 547 (2001).

[12] G. Auffermann, U. Schmidt, B. Bayer, Yu. Prots and R. Kniep, Anal. Bioanal. Chem. **373**, 880 (2002).

[13] R. J. Meier and R. B. Helmholdt, Phys. Rev. B **29**, 1387 (1984).

[14] J. J. Attema, G. A. De Wijs, G.R. Blake, and R. A. de Croot, J. Am. Chem. Soc. **125**, 16325 (2005).

[15] J. J. Attema, G A. De Wijs, and R. A. de Groot**,** J. Phys.: Condens. Matter. **19**, 165203, (2007).

[16] J. Winterlik, G. H. Fecher, C. Felser, C. Mühle, and Martin Jansen, J. Am. Chem. Soc. **129**, 6990 (2007).

[17] O. Volnianska and P. Bogusławski, Phys. Rev. B **77**, 220403 (R).(2008).

[18] H. Pan, J. B. Yi, L. Shen, R. Q. Wu, J. H. Yang, J. Y. Lin, Y. P. Feng, J. Ding, L. H. Van, and J. H. Yin, Phys. Rev. Lett. **99**, 127201 (2007)]

[19] X. J. Ye, H. A. Song, W. Zhong, M. H. Xu, X. S. Qi, C. Q. Jin, Z. X. Yang, C. T. Au, and Y. W. D, J.Phys. D:Appl. Phys. **41**, 155055 (2008).

[20] C. F. Yu, T.J. Lin, S.J. Sun, and H. Chou, J. Phys. D **40**, 6497 (2007).

[21] I. S. Elfimov, A. Rusydi, S. I. Csiszar, Z. Hu, H. H. Hsieh, H.-J. Lin, C. T. Chen, R. Liang, and G. A. Sawatzky, Phys. Rev. Lett. **98**, 137202 (2007).

[22] L. Shen, R. Q. Wu, H. Pan, G. W. Peng, M. Yang, Z. D. Sha, and Y. P. Feng, Phys. Rev. B **78**, 073306 (2008).

[23] K. Kenmochi, V. A. Dinh, K. Sato, A. Yanase, and H. Katayama-Yoshida, J. Phys. Soc. Jpn. **73**, 2952 (2004).

[24] T. Dietl, H. Ohno, F. Matsukura, J. Cibert, and D. Ferrand, Science **287**, 1019 (2000).

[25] T. Dietl, J. Appl. Phys. **103**, 07D111 (2008).

[26] K. Sato and Katayama-Yoshida, Jpn. J. Appl. Phys., Part 2 **39**, L555 (2000).

[27] M. S. Park and B. I. Min, Phys. Rev. B **68**, 224436 (2003).

[28] C. H. Chien, S.H. Chiou, G Y. Gao Y. D. Yao, J. Magn. Magn. Mater. **282**, 275 (2004).

[29] K. Ando, H. Saito, Zhengwu Jin, T. Fukumura, M. Kawasaki, and Y. Matsumoto, J. Appl. Phys. **89**, 7284 (2001).

[30] H. J. Lee, B. S. Kim, C. R. Cho, and S. Y. Jeong, Phys. Status Solidi B **241**, 1533 (2004).

[31] D. B. Buchholz, R. P. H. Chang, J. H. Song, and J. B. Ketterson, Appl. Phys. Lett. **87**, 082504 (2005).

[32] D. J. Keavney, D. b. Buchholz, Q. Ma, and R. P. H. Chang, Appl. Phys. Lett. **91**, 012501 (2007).

[33] Q. Xu, H. Schmidt, S. Zhou, K Potzger, M. Helm, H. Hochmuth, M. Lorenz, A. Setzer, P. Esquinazi, Ch. Meinecke, and M. Grundmann, Appl. Phys. Lett. **92**, 082508 (2008).

[34] S. Deng, K. P. Loh, J. B. Yi, J. Ding, H. R. Tan, M. Lin, Y. L. Foo, M. Zheng, and C. H. Sow, Appl. Phys. Lett. **93**, 193111 (2008).

[35] R. Q. Wu, G. W. Peng, L. Liu, Y. P. Feng, Z. G. Huang, and Q. Y. Wu, Appl. Phys. Lett. **89**, 062505 (2006).

[36] J. H. Lee, I. H. Choi, S. Shin, S. Lee, J. Lee, C. Whang, S. C. Lee, K. R. Lee, J. H. Baek, K. H. Chae, and J. Song, Appl. Phys. Lett. **90**, 032504 (2007).

[37] D. Huang, Yu. J. Zhao, D. H. Chen, and Yu. Z. Shao, Appl. Phys. Lett. **92**, 182509 (2008).

[38] L. H. Ye, A. J. Freeman, and B. Delley, Phys Rev. B **73**, 033203 (2006).

[39] L. M. Huang, A. l. Rosa, and R. Ahuja, Phys. Rev. B **74**, 075206 (2006).

[40] C. Sudakar, K. Padmanabhan, R. Naik, G. Lawes, B. J. Kirby, S. Kumar, and V. M. Naik, Appl. Phys. Lett. **93**, 042502 (2008).

[41] P. Esquinazi, A. Setzer, R. Hohne, C. Semmelhack, Y. Kopelevich, D. Spemann, T. Butz, B. Kohlstrunk, and M. Losche, Phys. Rev. B **66**, 024429 (2002).

[42] P. Esquinazi, D. Spemann, R. Hohne, A. Setzer, K.-H. Han, and T. Butz, Phys. Rev. Lett. **91**, 227201 (2003).

[43] H. Ohldag, T. Tyliszczak, R. Hohne, D. Spemann, P. Esquinazi, M. Ungureanu, and T. Butz, Phys. Rev. Lett. **98**, 187204 (2007).

[44] S. Talapatra, P. G. Ganesan, T. Kim, R. Vajtai, M. Huang, M. Shima, G. Ramanath, D. Srivastava, S. C. Deevi, and P. M. Ajayan, Phys. Rev. Lett. **95**, 97201 (2005).

[45] T. L. Makarova, B. Sundquist, R. Hohne, P. Esquinazi, Y. Kopelevich, P. Scharff, V. A. Davidov, L. S. Kashevarova, and A. V. Rakhmanina, Nature **413,** 716 (2001).

[46] R. A. Wood, M. H. Lewis, M. R. Lees, S. M. Bennington, M. G. Cain and N. Kitamura, J. Phys.: Condens. Matter **14**, L385 (2002).

[47] B. Narymbetov, A. Omerzu, V. V. Kabanov, M. Tokumoto, H. Kobayashi, and D. Michailovic, Nature **407,** 883 (2000).

[48] F. Simon, H. Kuzmany, B. Nafradi, T. Feher, L. Forro, F. Fulop, A. Janossy, L. Korecz, A. Rockenbauer, F. Hauke, and A. Hirsch, Phys. Rev. Lett. 97, 136801 (2006).

[49] J. Zhao, C. Zeng, X. Cheng, K. Wang, G. Wang, J. Yang, J. G. Hou, and Q. Zhu, Phys. Rev. Lett. **95**, 045502 (2005).

[50] M. J. Butcher, F. H. Jones, P. H. Beton, P. Moriaty, B. N. Cotier, and M. D. Upward, Phys. Rev. Lett **83**, 3478 (1999).

[51] W. Hearneit, C. Boehme, S. Schaefer, K. Huebener, K. Fostiropoulos, and L. Lips, Phys. Rev. Lett. 98, 216601(2007).

[52] Chih-Kai Yang, Appl. Phys. Lett. **92**, 033103 (2008).

[53] N. Parkansky, B. Alterkop, R. L. Boxman, G. Leitus, O. Berkh, Z. Barkay, Yu. Rosenberg, and N. Eliaz, Carbon **46**, 215 (2008).

[54] For a review, see S. J. Blundell and F. L. Pratt, J. Phys.: Condens. Matter **16,** R771 (2004).

[55] P. O. Lehtinen, A. S. Foster, Y. Ma, A. V. Krasheninnikov, and R. M. Nieminen, Phys. Rev. Lett. **93**, 187202 (2004).

[56] P. O. Lehtinen, A. V. Krasheninnikov, A. S. Foster, and R. M. Nieminen, in "Carbon-Based Magnetism", ed. T. Makarova and F. Palacio, Elsevier 2006, p. 371.

[57] Y. Zhang, S. Talapatra, S. Kar, R. Vajtai, S. K. Nayak, and P. M. Ajayan, Phys. Rev. Lett. **99**, 107201 (2007).

[58] Young-Woo Son, Marvin L. Cohen, Steven G. Louie, Nature **444**, 347 (2006).

[59] I. S. Elfimov, S. Yunoki, and G. A. Sawatzky, Phys. Rev. Lett. **89**, 216403 (2002).

[60] J. Osorio-Guille´n, S. Lany, S. V. Barabash, and A. Zunger, Phys. Rev. Lett. **96,** 107203 (2006).

[61] Haowei Peng, H. J. Xiang,Su-Huai Wei, Shu-Shen Li, Jian-Bai Xia, and Jingbo Li, Phys. Rev. Lett. **102**, 017201 (2009).

[62] T. A. Kennedy, N. D. Wilsey, J. J. Krebs, and G. H. Stauss, Phys. Rev. Lett. **50**, 1281 (1983).

[63] L. E. Halliburton, Phys. Rev. B **8**, 1610 (1973).

[64] B. H. Rose and L. E. Halliburton, J. Phys. C 7, 3981 (1974).

[65] D. Galland and A. Herve, Phys. Lett. **33** A,1 (1970).

[66] S. M. Evans, N. C. Giles, L. E. Halliburton, and L. A. Kappers, J. Appl. Phys. 103, 043710 (2008).

[67] H. Itoh, A. Kawasuso, T. Ohshima, M. Yoshikawa, I. Nashiyama, S. Tanigawa, S. Misawa, H. Okumura, and S. Yoshida, Phys. Stat. Sol. (a) **162,** 173 (1997).

[68] L. Torpo, R. M. Nieminen, K.E. Laasonen, and S. Poykko. Appl. Phys. Lett. **74** (2), 221 (1999).

[69] O.Volnianska and P. Boguslawski, XXXVII International School on the Physics of Semiconducting Compounds Jaszowiec 2008, p. 144.

[70] P. Dev, Y. Xue, and P. Zhang, Phys. Rev. Lett. **100**, 117204 (2008).

[71] A. Drogetti, C. D. Pemmaraju, and S. Sanvito, Phys. Rev. B **78**, 140404 (R) (2008).

[72] P. Hohenberg and W. Kohn, Phys. Rev. **13**6, B864 (1964).

[73] W. Kohn and L. J. Sham, Phys. Rev. **14**0, A1133 (1965).

[74] W. Kohn, Rev. Mod. Phys. **71**, 1253 (1999).

[75] R. G. Parr, W. Yang, *Density-Functional Theory of Atoms and Molecules*. Oxford: Oxford University Press. (1994).

[76] M. Ceperley and B. J. Alder, Phys. Rev. Lett. **45,** 566 (1980).

[77] J. P Perdew, A. Zunger, Phys. Rev. B **23** (10), 5048 (1981).

[78] D.C. Langreth and J.P. Perdew, Phys. Rev. B **21**, 5469 (1980).

[79] J. P. Perdew, J. A. Chevary, S. H. Vosko, K. A. Jackson, M. R. Pederson, D. J. Singh, and C. Fiolhais, Phys. Rev. B **46**, 6671 (1992).

[80] J. P. Perdew, K. Burke, and M. Ernzerhof, Phys. Rev. Lett.**77**, 3865 (1996).

[81] D. R. Haman, M. Schluter, and C. Chiang, Phys. Rev. Lett. **43**, 1494 (1979).

[82] D. Vanderbilt, Phys. Rev. B **41**, 7892 (1990).

[83] www.pwscf.org.

[84] H. J. Monkhorst and J. D. Pack, Phys. Rev. B **13**, 5188 (1976).

[85] M. Mizuguchi, H. Akinaga, T. Manago, K. Ono, M. Oshima, M. Shirai, M. Yuri, H. J. Lin, H. H. Hsieh, and C. T. Chen, J. Appl. Phys. **91**, 7917 (2002).

[86] J. H. Zhao, F. Matsukura, K. Takamura, E. Abe, D. Chiba, and H. Ohno, Appl. Phys. Lett. **79**, 2776 (2001).

[87] J. E. Pask, L. H. Yang, C. Y. Fong, W. E. Pickett, and S. Dag, Phys. Rev. B **67**, 224420 (2003).

[88] H. F. George and H. K. John, Phys. Rev. **93**, 1004 (1954).

[89] D. Gall, I. Petrov, N. Hellgren, L. Hultman, J. E. Sundgren, and J. E. Greene, J. Appl. Phys. **84**, 6034 (1998).

[90] T.-Y. Lee, D. Gall, C.-S. Shin, N. Hellgren, I. Petrov, and J. E. Greene, J. Appl. Phys. **94**, 921 (2003).

[91] J. R. Frederick and D. Gall, J. Appl. Phys. **98**, 054906 (2005).

[92] K. Suzuki, T. Kaneko, H. Yoshida, Y. Obi, H. Fujimori, and H. Morita, J. Alloys Compd. **306**, 66 (2000).

[93] H. Yang, H. Al-Brithen, A. R. Smith, J. A. Borchers, R. L. Cappelletti, and M. D. Vaudin, Appl. Phys. Lett. **78**, 3860 (2001).

[94] W. R. L. Lambrecht, M. Prikhodko, and M. S. Miao, Phys. Rev. B **68**, 174411 (2003).

[95] B. R. Sahu and L. Kleinman, Phys. Rev. B **68**, 113101 (2003).

[96] A. Janotti, S. H. Wei, and L. Bellaiche, Appl. Phys. Lett. **82**, 766 (2003).

[97] P. Bogusławski and J. Bernholc, Appl. Phys. Lett. **88**, 092502 (2006).

[98] We do not consider other AFM phases since, *e. g*., in *zb*-MnTe energies of type-I and type-III AFM orders differ by 2 meV/atom only, see P. Djemia, Y. Roussigné, A. Stashkevich, W. Szuszkiewicz, N. Gonzalez Szwacki, E. Dynowska, E. Janik, B. J. Kowalski, G. Karczewski, P. Bogusławski, M. Jouanne, and J. F. Morhange, Acta Phys. Polonica A, **106**, 239 (2004). Similar results are expected for II-V compounds. This value is an order of magnitude smaller than $\Delta E^{\text{FM-AFM}}$ for CaN and SrN, and thus does not affect our conclusions.

[99] D.H. Martin, Magnetism in Solids, 1llife, London (1967).

[100] V. A. Gubanov, A. I. Liechtenstein, and A. V. Postnikov, *Magnetism and the Electronic Structure of Crystals* (Springer, Berlin, 1992).

[101] D. Ceperley, Nature **397**, 386 (1999).

[102] G. Ortiz, M. Harris, and P. Ballone, Phys. Rev. Lett. **82**, 5317 (1999).

[103] N. Takeuchi, Phys. Rev. B **65**, 045204 (2002).

[104] J. C. Crowhurst, A. F. Goncharov, B. Sadigh, Ch. L. Evans, P. G. Morrall, J. L. Ferreira, and A. J. Nelson, Science **311**, 1275 (2006).

[105] A. Tabata, A. P. Lima, L. K. Teles, L. M. R. Scolfaro, J. R. Leite, V. Lemos, B. Schottker, T. Frey, D. Schikora, and K. Lischka, Appl. Phys. Lett. **74**, 362 (1999).

[106] A. F. Young, C. Sanloup, E. Gregoryanz, S. Scandolo, R. J. Hemley, and H. Mao, Phys. Rev. Lett. **96,** 155501 (2006).

[107] R. Yu, Q. Zhan, and X. F. Zhang, Appl. Phys. Lett. **88**, 051913 (2006).

[108] D. Iusan, B. Sanyal, and O.Eriksson, Phys. Rev. B **74**, 235208 (2006).